AIAA JOURNAL
Vol. 48, No. 3, March 2010

Hybrid Reynolds-Averaged/Large-Eddy Simulations of a Coaxial Supersonic Freejet Experiment

R. A. Baurle*
NASA Langley Research Center, Hampton, Virginia 23681
and
J. R. Edwards†
North Carolina State University, Raleigh, North Carolina 27695

DOI: 10.2514/1.43771

Reynolds-averaged and hybrid Reynolds-averaged/large-eddy simulations have been applied to a supersonic coaxial jet flow experiment. The experiment was designed to study compressible mixing flow phenomenon under conditions that are representative of those encountered in scramjet combustors. The experiment used either helium or argon as the inner jet nozzle fluid, and the outer jet nozzle fluid consisted of laboratory air. The inner and outer nozzles were designed and operated to produce nearly pressure-matched Mach 1.8 flow conditions at the jet exit. The purpose of the computational effort was to assess the state of the art for each modeling approach and to use the hybrid Reynolds-averaged/large-eddy simulations to gather insight into the deficiencies of the Reynolds-averaged closure models. The Reynolds-averaged simulations displayed a strong sensitivity to choice of turbulent Schmidt number. The initial value chosen for this parameter resulted in an overprediction of the mixing layer spreading rate for the helium case, but the opposite trend was observed when argon was used as the injectant. A larger turbulent Schmidt number greatly improved the comparison of the results with measurements for the helium simulations, but variations in the Schmidt number did not improve the argon comparisons. The hybrid Reynolds-averaged/large-eddy simulations also overpredicted the mixing layer spreading rate for the helium case, while underpredicting the rate of mixing when argon was used as the injectant. The primary reason conjectured for the discrepancy between the hybrid simulation results and the measurements centered around issues related to the transition from a Reynolds-averaged state to one with resolved turbulent content. Improvements to the inflow conditions were suggested as a remedy to this dilemma. Second-order turbulence statistics were also compared with their modeled Reynolds-averaged counterparts to evaluate the effectiveness of common turbulence closure assumptions.

Nomenclature

a	=	speed of sound
C_d	=	dissipation constant for turbulence kinetic energy
C_s	=	Smagorinsky constant for turbulent viscosity
C_μ	=	constant for turbulent viscosity
D	=	center jet diameter
d	=	distance to nearest solid surface
F	=	hybrid blending function
h	=	static enthalpy
k	=	turbulence kinetic energy
ℓ	=	turbulence length scale (Taylor microscale)
P	=	pressure
P_k	=	production term for turbulence kinetic energy
Pr_t	=	turbulent Prandtl number
Sc_t	=	turbulent Schmidt number
T	=	temperature
u, v, w	=	Cartesian velocity components
x, r, θ	=	cylindrical coordinates
x, y, z	=	Cartesian coordinates
Y_m	=	mass fraction of species m
y^+	=	nondimensional law-of-the-wall coordinate
α	=	blending function constant
Δ	=	subgrid scale filter width
δ_{ij}	=	Kronecker delta
η	=	blending function length scale ratio
κ	=	von Karman constant or MUSCL parameter
μ	=	molecular viscosity
μ_t	=	turbulent viscosity
ρ	=	density
ω	=	specific turbulence dissipation rate

Subscripts

air	=	coflow air index
i, j, k	=	computational coordinate indices
inj	=	center jet injectant index

Presented as Paper 129 at the 47th AIAA Aerospace Sciences Meeting including The New Horizons Forum and Aerospace Exposition, Orlando, FL, 5–8 January 2009; received 12 February 2009; revision received 3 June 2009; accepted for publication 10 September 2009.

*Aerospace Engineer, Hypersonic Airbreathing Propulsion Branch. Associate Fellow AIAA.

†Professor, Mechanical and Aerospace Engineering Department. Associate Fellow AIAA.

Introduction

REYNOLDS-AVERAGED computational fluid dynamics (CFD) models have become an integral part of the design and analysis of high-speed airbreathing engines. The maturation of multipurpose CFD codes coupled with advancements in computer architectures have substantially reduced the turnaround time required to perform steady-state Reynolds-averaged simulations (RAS). Unfortunately, the turbulence models required to close the Reynolds-averaged equation set have not kept pace with these advancements. As a result, RAS approaches often require calibrations for key model parameters. One example is given in [1], in which variations of the turbulent Prandtl and Schmidt numbers for a scramjet combustor simulation were shown to produce outcomes that ranged from engine unstart to complete flame blowout. Similar examples that illustrate solution sensitivities to unknown RAS modeling parameters can be found in [2,3].

Large-eddy simulation (LES) methods have the potential to reduce the modeling sensitivity inherent to RAS approaches, because the

intent of LES is to resolve the large-scale turbulent structures while modeling only the small scales. Regrettably, the computational expense of wall-resolved LES (particularly when applied to configurations of interest to the high-speed propulsion community) is well beyond what can be deemed as practical by today's standards. Hybrid RAS/LES approaches offer some relief to the computational costs associated with LES. These methodologies allow LES content to be resolved in areas that require a more rigorous modeling approach, while maintaining a more cost effective RAS approach for benign regions of the flow (e.g., attached boundary layers). Hybrid approaches first appeared in the literature a decade ago [4,5], and although many advancements have been made since then, the modeling is far from mature (as evidenced by the vast array of hybrid approaches that have appeared in recent years [6–9]). The computational expense required for a hybrid simulation, although less than that of a full LES, is still formidable when compared with steady-state RAS.

The present effort uses both RAS and hybrid RAS/LES approaches to model a series of supersonic coaxial jet experiments [10,11] that have been studied at the NASA Langley Research Center. These experiments involve the coaxial injection of either helium or argon into air. CFD simulations (based on RAS approaches) have previously been performed to augment the measurements in the works referenced previously. Additional RAS data were gathered in this effort to ensure that consistent practices were employed for the comparisons made with hybrid RAS/LES results. The specific goals of this computational effort are as follows:

1) Assess the capabilities of RAS and hybrid RAS/LES for predicting high-speed mixing layers.

2) Determine the model sensitivities for both RAS and hybrid RAS/LES approaches.

3) Attempt to use the hybrid RAS/LES results to assess the appropriateness of models used by RAS.

Measured values of composition, pitot pressure, velocity, and rms of the velocity fluctuation are available for comparison with the simulations. Additional higher-order correlations (that are difficult to obtain experimentally) are extracted from the hybrid RAS/LES results and compared with the RAS predictions. The correlations considered include the Reynolds stress tensor and the Reynolds mass flux vector.

Geometry Description and Flow Conditions

A schematic of the coaxial nozzle assembly is shown in Fig. 1. The injectant supplied to the center jet nozzle was either a mixture of 95% helium and 5% oxygen (by volume) or pure argon. In the former case, a trace amount of oxygen was added to allow for the measurement of the streamwise component of velocity using the Raman excitation plus laser-induced electronic fluorescence (RELIEF) [12] oxygen flow tagging technique. The internal diameter of the center jet nozzle is 10 mm at the nozzle exit. The centerbody that forms the internal nozzle is 0.25 mm thick at the nozzle exit, providing a small blunt base to anchor the shear layer formed between the two nozzle streams. The coflow air nozzle has an internal diameter of 60.47 mm, and the outer surface of this nozzle extends 12.66 mm downstream of the centerbody. The 38.6 deg juncture between the internal surface of the coflow nozzle and the conical exterior surface is sharp. Hence, there is no appreciable base region to segregate the outer jet flow from the surrounding ambient air. Further details concerning the geometry of the rig, and the methodology used for its design, can be found in [10].

The nominal flow conditions for each experiment are given in Tables 1 and 2, along with the cited uncertainties [10,11]. The thermocouples used to measure the jet temperatures were located in the gas supply lines, and the pressure taps used to measure the operating pressures were positioned as shown in Fig. 1. Both nozzle streams have a design Mach number of 1.8. The flow velocity exiting the inner jet nozzle, however, is markedly different for each case, due to the disparate molecular weights of each center jet injectant. The velocity of the center jet is more than twice that of the coflow jet for the helium case (case 1), but it is 16% lower than that of the coflow jet for the argon case (case 2). An estimation of the convective Mach number [13]

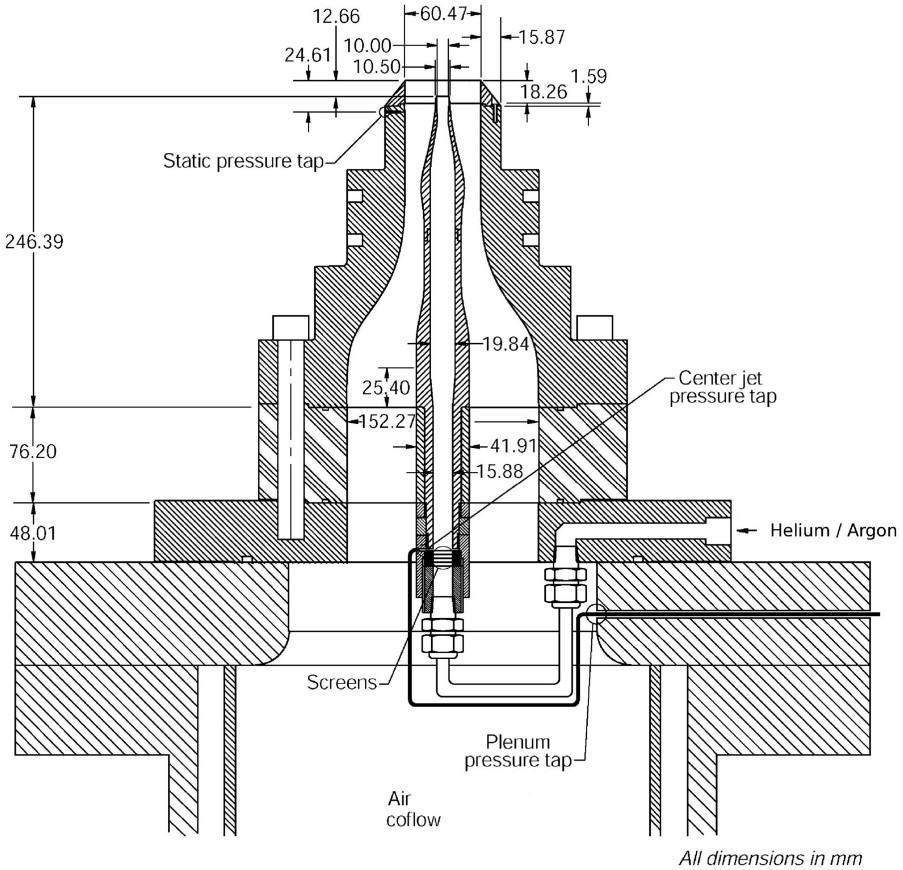

Fig. 1 Schematic of the coaxial nozzle assembly.

Table 1 Case 1: Helium–air test conditions

Nominal conditions	Center jet	Coflow jet	Ambient
Mach number	1.8[a]	1.8[a]	0.025[b]
Total temperature, K	305.0 (±9)	300.0 (±6)	294.6 (±6)
Total pressure, kPa	614.93 (±6)	579.80 (±4)	101.325 (±1)

[a]Nozzle design Mach number
[b]Value assumed for the entrained ambient flow

Table 2 Case 2: Argon–air test conditions

Nominal conditions	Center jet	Coflow jet	Ambient
Mach number	1.8[a]	1.8[a]	0.025[b]
Total temperature, K	297.9 (±3.5)	294.3 (±3.5)	294.6 (±3.5)
Total pressure, kPa	615.86 (±5.5)	580.68 (±4.4)	101.325 (±0.6)

[a]Nozzle design Mach number
[b]Value assumed for the entrained ambient flow

$$\frac{|u_{\text{air}} - u_{\text{inj}}|}{a_{\text{air}} + a_{\text{inj}}} \tag{1}$$

yields a value of 0.7 for case 1 and 0.16 for case 2, respectively. Hence, one expects compressibility effects to be prevalent in case 1, whereas case 2 is expected to behave more like an incompressible shear layer.

Computational Methodology

All computational results were obtained using the viscous upwind algorithm for complex flow analysis (VULCAN) software package. The code solves the unsteady conservation equations appropriate for calorically or thermally perfect gases with a cell-centered finite volume scheme. Efficient utilization of parallel architectures is realized through calls to message-passing interface routines using an single-program multiple-data paradigm; a natural choice for multiblock flow solvers. Arbitrary block-to-block (nonaligned) connectivity is also available, allowing the flexibility to add or remove grid points at zonal interfaces. A variety of upwind formulations are available for evaluating the inviscid fluxes, whereas central differences are used for the viscous fluxes. The primary solvers available for steady-state simulations are a diagonalized approximate factorization (DAF) scheme or a planar relaxation scheme that solves the planar linear system via an incomplete lower/upper (ILU) factorization. An explicit multistage Runge–Kutta or an implicit dual time-stepping strategy (using DAF or ILU) are the options available for unsteady applications. A variety of one-equation and two-equation turbulence models exist for RAS. LES and hybrid RAS/LES models are also available for turbulent flows that require a more rigorous modeling effort. Further details describing the code are found elsewhere [14,15].

Reynolds-Averaged Simulation Numerical Model Description

The RAS results used the low-diffusion flux split scheme of Edwards [16] to evaluate the inviscid fluxes. The monotone upstream-centered scheme for conservation laws (MUSCL) extrapolation parameter κ was chosen as $\frac{1}{3}$ to minimize spatial truncation error, and the van Leer flux limiter [17] was employed to enforce the total variation diminishing (TVD) property. All of the steady-state RAS solutions were advanced in time with a DAF scheme.

Reynolds-Averaged Simulation Physical Model Description

The turbulence model chosen was the Wilcox k-ω model [18], and the wall function procedure of Wilcox [19] was used to relax the grid spacing requirements near solid surfaces. A dilatation–dissipation modification [18] to the turbulence kinetic energy equation was also enabled to reduce the shear layer spreading rate that has been observed under high compressible Mach number conditions. The baseline values for the turbulent Prandtl Pr_t and Schmidt Sc_t numbers, which control the turbulent transport of energy and mass, were chosen as 0.9 and 0.5, respectively. The turbulent Schmidt number was one of the properties that was varied in parametric studies to evaluate the sensitivity of the RAS solutions to the value assumed for this coefficient.

Hybrid Reynolds-Averaged/Large-Eddy Simulation Numerical Model Description

The hybrid RAS/LES results required a somewhat different algorithmic approach to encourage the development of resolved turbulent content. In particular, the standard TVD limiters that are typically employed for RAS are overly dissipative when used for LES. This class of limiter tends to locally reduce the accuracy of the inviscid flux scheme to first-order whenever extrema of any magnitude are encountered. Essentially nonoscillatory (ENO) limiters offer a simple means of maintaining second-order accuracy near local extrema. This is accomplished by using data at additional grid nodes to alter the stencil used to construct the inviscid flux terms. The ENO limiter used in this effort is the SONIC-A limiter of Suresh and Huynh [20], which can be considered as a second-order extension of the van Leer TVD limiter. All of the time-accurate hybrid RAS/LES solutions were advanced in time using a dual time-stepping approach that combined the DAF scheme for integration in pseudotime, with a three-point backward finite difference approximation for integration in real time. The values selected for the physical time step and subiteration CFL constraint were 0.05 μs and 50.0, respectively. The time step was chosen based on cell residence time considerations to ensure that turbulent structures would not traverse more than one grid cell per time step. The subiteration process was considered converged when the residual error dropped at least 2.5 orders of magnitude. This level of convergence typically required four to seven subiterations for each physical time step.

Hybrid Reynolds-Averaged/Large-Eddy Simulation Physical Model Description

The hybrid RAS/LES methodology used in this effort builds on the previous work discussed in [6]. This framework was designed to enforce a RAS behavior near solid surfaces and switch to an LES behavior in the outer portion of the boundary layer and free shear regions. Hence, this formulation can be thought of as a wall-modeled LES approach, for which RAS is used as the near-wall model. The basic idea is to blend any trusted RAS eddy viscosity with a desired LES subgrid scale (SGS) viscosity, along with any transport equations that involve a common RAS and SGS property. In this effort, the Wilcox k-ω RAS model [18] was blended with the one-equation SGS model of Yoshizawa and Horiuti [21]. The Yoshizawa model involves an evolution equation for the SGS turbulence kinetic energy; hence, the blended expressions that are appropriate for this model combination are

$$\begin{aligned}\text{Hybrid RAS/SGS viscosity} &= (F)[\text{RAS viscosity}] \\ &\quad + (1-F)[\text{SGS viscosity}]; \text{Hybrid RAS/SGS } k\text{-equation} \\ &= (F)[\text{RAS } k\text{-equation}] + (1-F)[\text{SGS } k\text{-equation}]\end{aligned} \tag{2}$$

where F is a blending function that varies between 0 and 1. Note that the transport equation for the RAS specific dissipation rate ω does not have an SGS counterpart. Hence, the blending is not applied to this equation, and all of the terms in this equation that involve the eddy viscosity are evaluated based on RAS relationships.

The motivation behind the development of this hybrid RAS/LES framework is twofold. First, the blending of two independent RAS and LES closure models offers the flexibility of having an optimized set of closure equations for both RAS and LES modes. The second (and more critical) driving factor was the desire to alleviate the difficulties associated with the design of grid topologies that are appropriate for purely grid-dependent blending paradigms, such as those used for detached eddy simulation (DES) [4,22]. The movement away from simple grid-dependent blending strategies has gained momentum in recent years [7,8]. In fact, even the developers of DES are now promoting an improved version of their scheme,

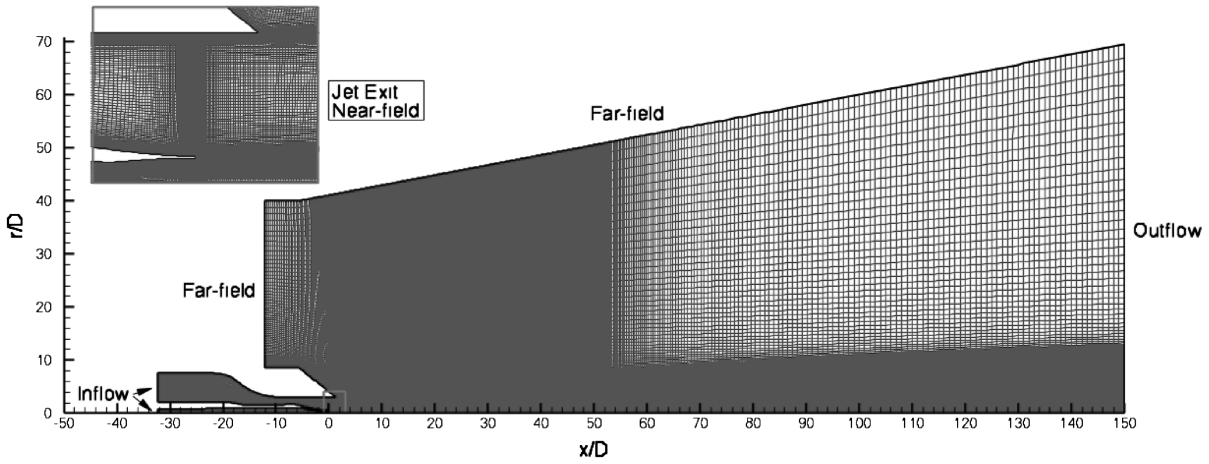

Fig. 2 Axisymmetric grid used for RAS (247,368 cells).

termed delayed DES [8], that involves flow-dependent functions to switch between RAS and LES regimes.

The blending function F used in this effort is based on the ratio of the wall distance d to a modeled form of the Taylor microscale ℓ:

$$F = \frac{1}{2}\left\{1 - \tanh\left[5\left(\frac{\kappa}{\sqrt{C_\mu}}\eta^2 - 1\right) - \phi\right]\right\}$$
$$\ell = \sqrt{\frac{\mu}{C_\mu \rho \omega}}; \qquad \eta = \frac{d}{\alpha \ell} \tag{3}$$

where κ is the von Karman constant (0.41), C_μ is 0.09, α is a user-defined model constant, and ϕ is set to $\tanh^{-1}(0.98)$ to force the balancing position of F (i.e., the position where $\kappa\eta^2 = \sqrt{C_\mu}$) to 0.99. The value chosen for α provides control over the y^+ position, where the average LES to RAS transition point (defined as $F = 0.99$) occurs. If resolved LES content is desired for an attached boundary layer, then this constant should be set, such that the transition point occurs in the region where the boundary layer wake law starts to deviate from the log law. If the transition point is enforced at a lower y^+ value (e.g., well within the log law region), a dual log layer can appear [23,24]. Conversely, if the transition point is enforced at a y^+ value that extends well into the defect layer, then the level of resolved turbulence will be limited. Details on a procedure to analytically determine the value for α that correspond to a target y^+ value are described in [24].

Grid and Boundary Condition Details

A two-dimensional (axisymmetric) grid was generated for the steady-state Reynolds-averaged solutions (see Fig. 2). This grid consisted of just under 250,000 cells divided across five structured grid zones. The computational domain extended 150 center jet diameters D downstream of the jet exit and between 40 and 70 jet diameters in the radial direction. The internal flowfield within the concentric nozzles was also included as part of the computational domain to allow for the development of boundary layers. The last experimental data stations were located at 26.101 (case 1) and 45.276 (case 2) jet diameters downstream of the center jet exit plane. Hence, most of the grid was clustered between the jet exit and an x/D of 50. The portion of the computational domain downstream of $x/D = 50$ was added to provide plenty of space for the jet flow to reach a subsonic state, which ensured that the specified pressure outflow boundary condition (with all other variables extrapolated) remained well posed. The far-field boundary was also placed many tens of jet diameters away from the domain of interest to minimize any chance of data corruption that could occur via wave reflections off of the characteristic inflow condition [25] that was applied along this boundary. The nozzle stagnation conditions given in Tables 1 and 2 were applied at each nozzle inflow plane, with the Mach number extrapolated from the interior to complete the specification of these subsonic inflow boundaries. The operating total temperature of each nozzle was nominally the same as the room temperature, and so all solid surfaces were assumed to be adiabatic no-slip surfaces. The grid was clustered to all solid surfaces at a level appropriate for the use of wall functions ($y^+ \leq 36$). Finally, the entire grid system was split up into a total of 179 grid blocks, which yielded excellent load balance statistics for up to 64 processors.

An azimuthal slice of the three-dimensional (3-D) grid generated for the hybrid RAS/LES cases is shown in Fig. 3. The boundary conditions and the extent (x and r) of the computational domain were identical to those used for the axisymmetric RAS cases. The gridding strategy, however, was altered to reflect the change in computational algorithm. LES requires the use of grid cells that are roughly

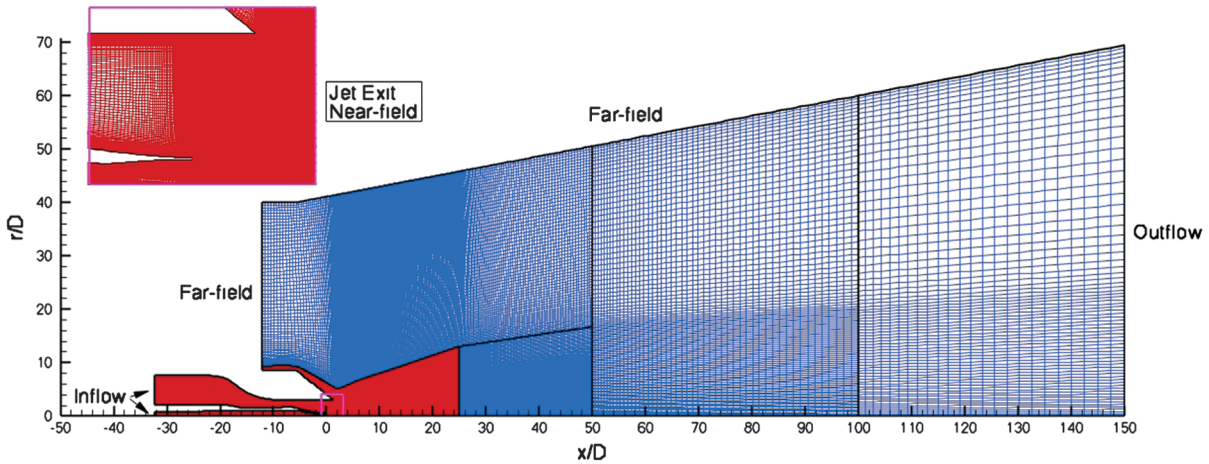

Fig. 3 Azimuthal slice of the 3-D grid used for hybrid RAS/LES (43,285,632 cells).

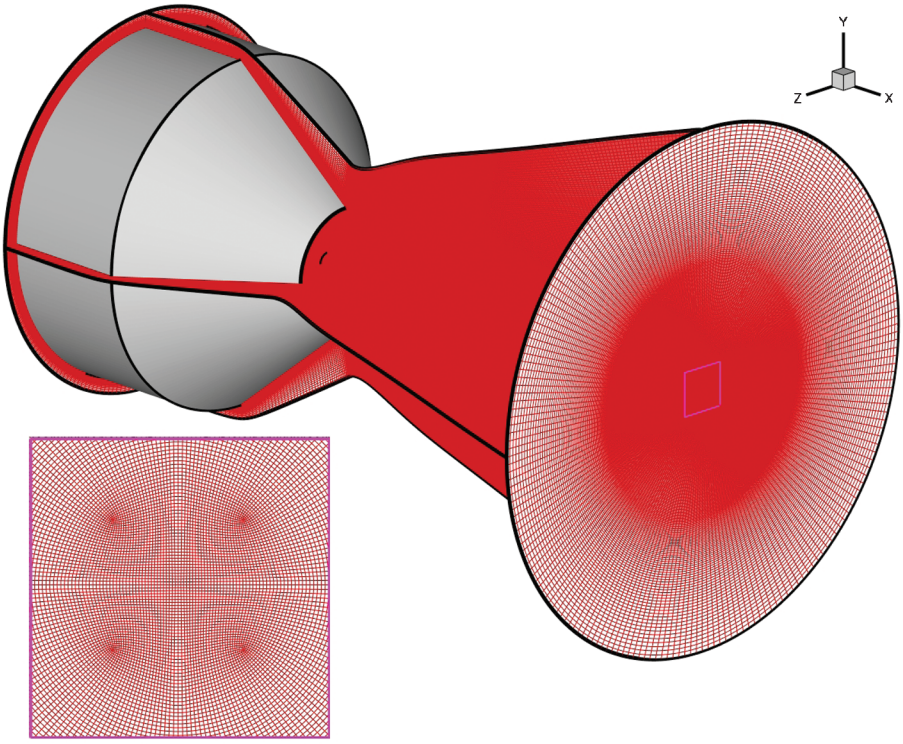

Fig. 4 Isometric visualization of the LES-resolved portion of the hybrid RAS/LES grid.

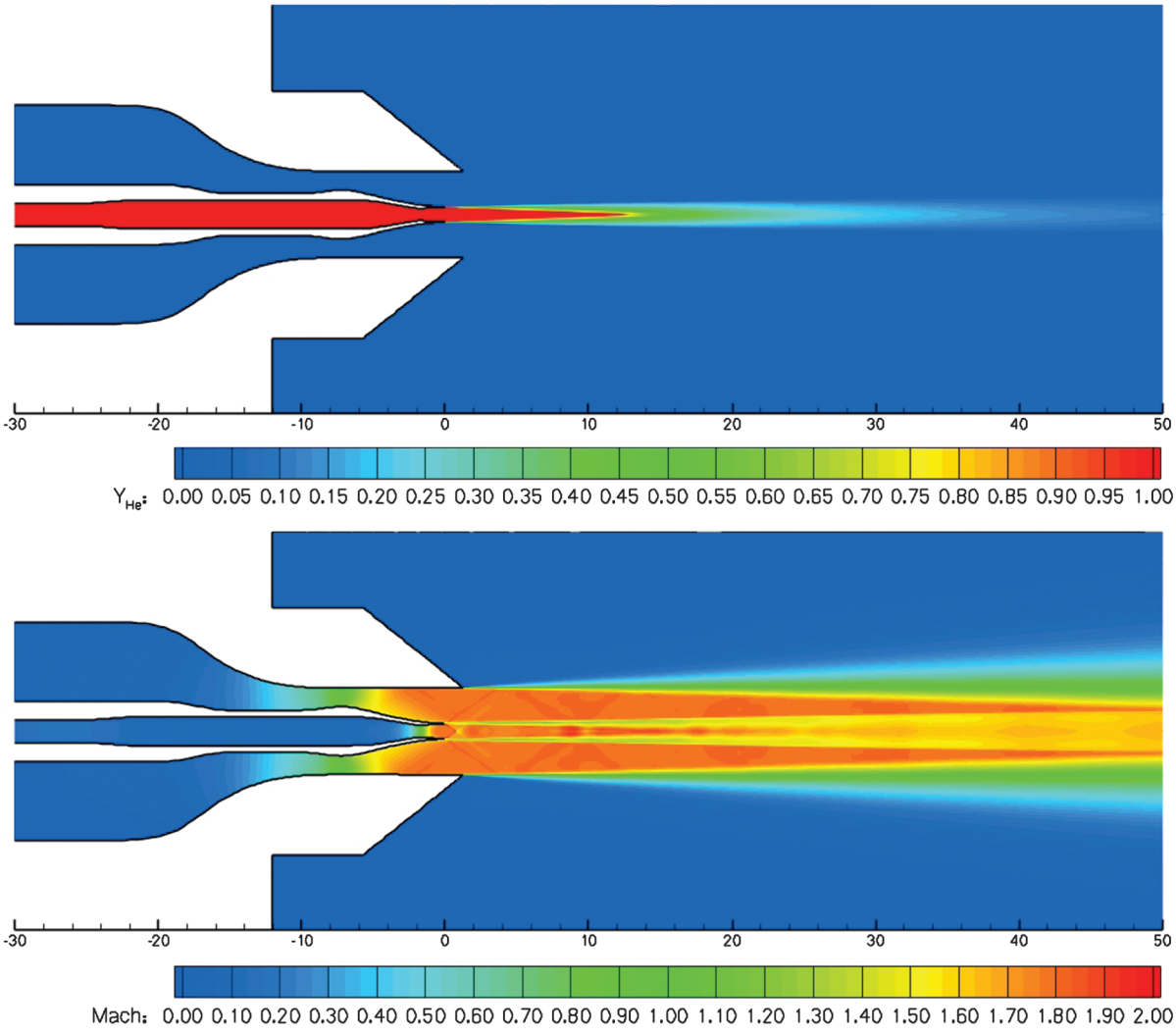

Fig. 5 Contours of normalized helium mass fraction and Mach number for the baseline RAS.

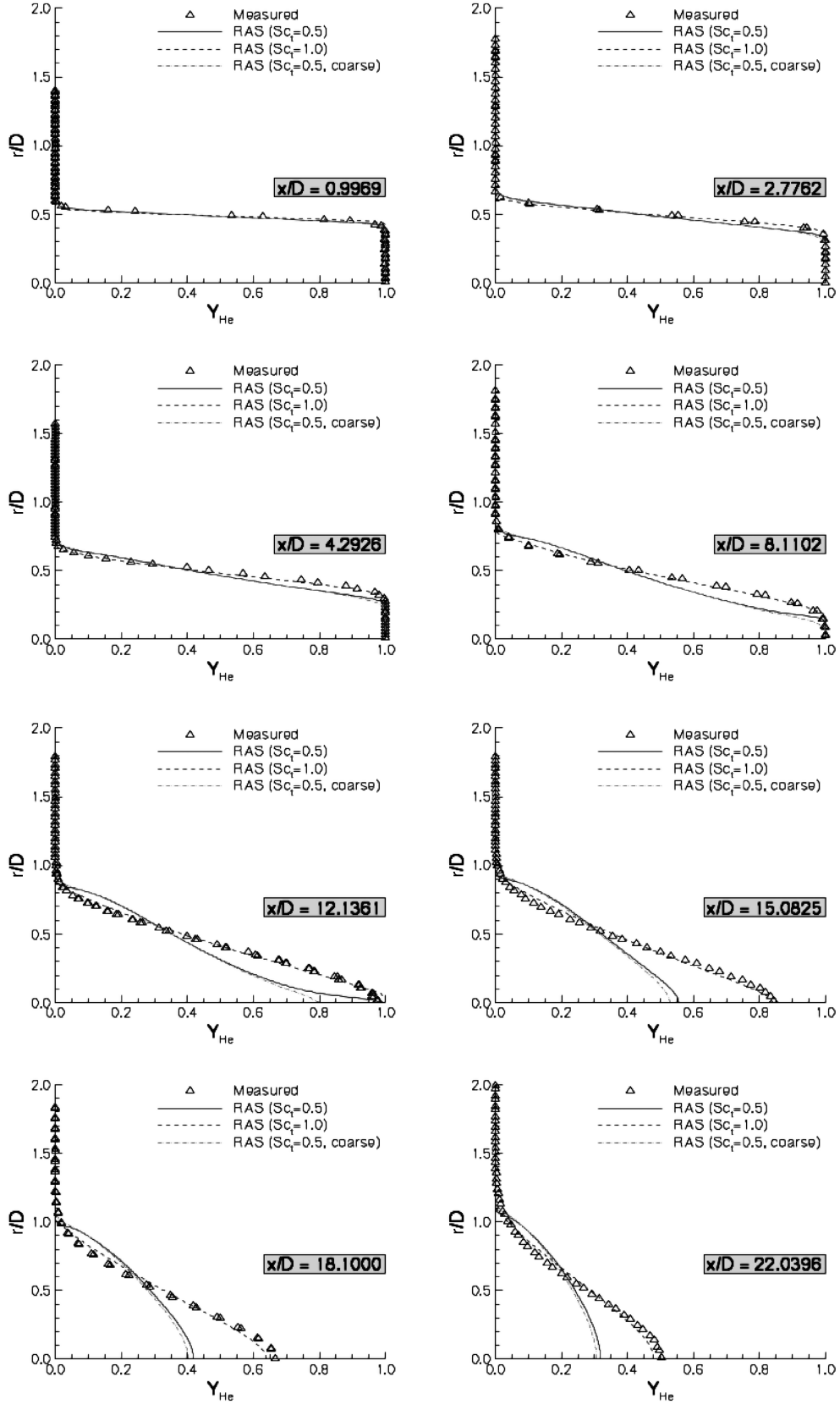

Fig. 6 Comparison of normalized helium mass fraction (RAS predictions) with measured values.

isotropic, to allow for the development and sustainment of resolved turbulent structures. Hence, the streamwise grid spacing had to be reduced from that used for the pure RAS. This requirement, coupled with the fact that the full 3-D flowfield must be solved, forced a concession to be made to keep the computational costs within reason. The compromise that was accepted was to provide a level of grid resolution capable of supporting LES only up to an x/D of 25 (highlighted in red). This domain captures all but the last experimental station for case 1, and 13 of the 16 stations for case 2. Nonaligned zonal interfaces (patches) were inserted at x/D stations of 25, 50, and 100 to systematically remove grid nodes in the radial direction. A patch interface was also inserted in the ambient air

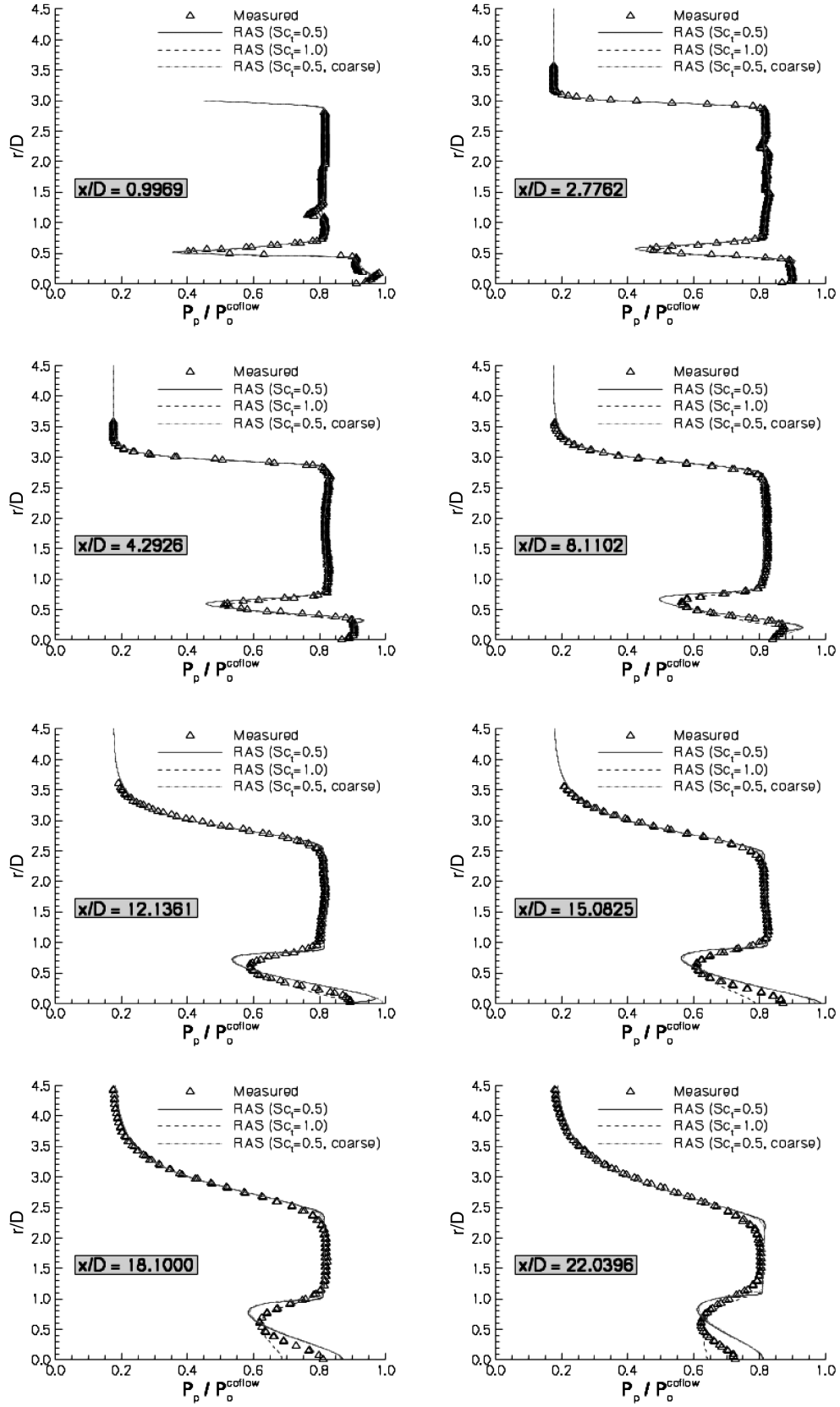

Fig. 7 Comparison of case 1 pitot pressure (RAS predictions) with measured values.

region to coarsen the streamwise spacing in the far field where axial refinement is not required. Each patch interface is denoted by a solid black line in Fig. 3. In addition to substantially reducing the computational costs, the coarsening process performed at large x/D tends to dissipate the large-scale vortical structures that propagate out of the LES domain of interest. This reduces the likelihood of an ill-posed boundary condition appearing at the outflow plane. A H–O mesh topology was chosen for the crossflow planes to avoid the numerical difficulties associated with the collapsed faces that would result from a classic polar topology. This feature of the grid is illustrated in the 3-D view of the LES domain shown in Fig. 4. Finally, the entire grid system (43,285,632 cells) was split up into a

total of 1669 grid blocks, which resulted in excellent load balance statistics for up to 360 processors.

Reynolds-Averaged Results

Contours of the helium mass fraction and Mach number extracted from the baseline RAS ($Sc_t = 0.5$) are shown in Fig. 5. The helium mass fractions have been normalized by the center jet value (95% by volume corresponds to 70.39% by mass):

$$Y_{\mathrm{He}} \Rightarrow Y_{\mathrm{He}}/0.7039 \tag{4}$$

for all of the results that follow to simplify the analysis and comparisons with the argon cases. The helium contours show that the potential core of the center jet persists for approximately 12 jet diameters, and the centerline helium mass fraction in the plume that forms downstream of this station decays to a value of 0.115 at an $x/D = 50$. The Mach contours show that both nozzle streams are nearly pressure-matched. Although not visible at this scale, a pair of counter-rotating separation bubbles are present behind the small blunt base of the centerbody. The weak expansion fan that is seen on either side of the base region forms as the jets negotiate around this separated flow zone. A weak recompression shock then develops as the flow is forced to turn back on itself at the close-off point of the recirculation bubble. The conical recompression shock that formed in the center jet flowfield steepens as it approaches the axis of symmetry, resulting in a Mach disk at the axis. As will be shown later, the total pressure loss that occurs across this shock wave is also evident in the measured pitot pressure surveys.

Measured helium mass fraction profiles are compared with the RAS results in Fig. 6. The measurements of injectant composition were made using a gas sampling probe, as detailed in [10]. In general, the $Sc_t = 0.5$ simulation overpredicted the rate of mixing between the coaxial streams. Hence, an additional simulation was performed with the Sc_t value increased by a factor of two (to 1.0). The third result shown in this figure was obtained from a coarse grid simulation (factor of two coarsening in each coordinate direction) that used an Sc_t value of 0.5. Comparisons are made at eight axial stations downstream of the center jet exit plane. The results extracted from the $Sc_t = 0.5$ simulation overpredicted the measured growth rate of the mixing layer for all but the first experimental station. This feature is illustrated by the wider mixing width between the two streams (as compared with the measurements) and leads to a premature close off of the potential core of the helium jet. It should be noted that the RAS model used in this effort included a dilatation–dissipation modification [18] to reduce the shear layer spreading rate for compressible mixing layers. This leaves the turbulent Schmidt number (which controls the rate of turbulent mass diffusion) as the remaining parameter that can be adjusted to reduce the mixing rate. The results obtained when doubling the Sc_t value (which reduces the modeled turbulent diffusion term by a factor of two) agree well with the measurements. In fact, the results obtained with $Sc_t = 1.0$ matched nearly every measured result to within the precision of the measurement device of ± 1.0–1.5%. The effect of coarsening the grid resolution had a much smaller impact on the predicted results, indicating that the level of grid convergence is well within the uncertainty bounds of the physical models employed.

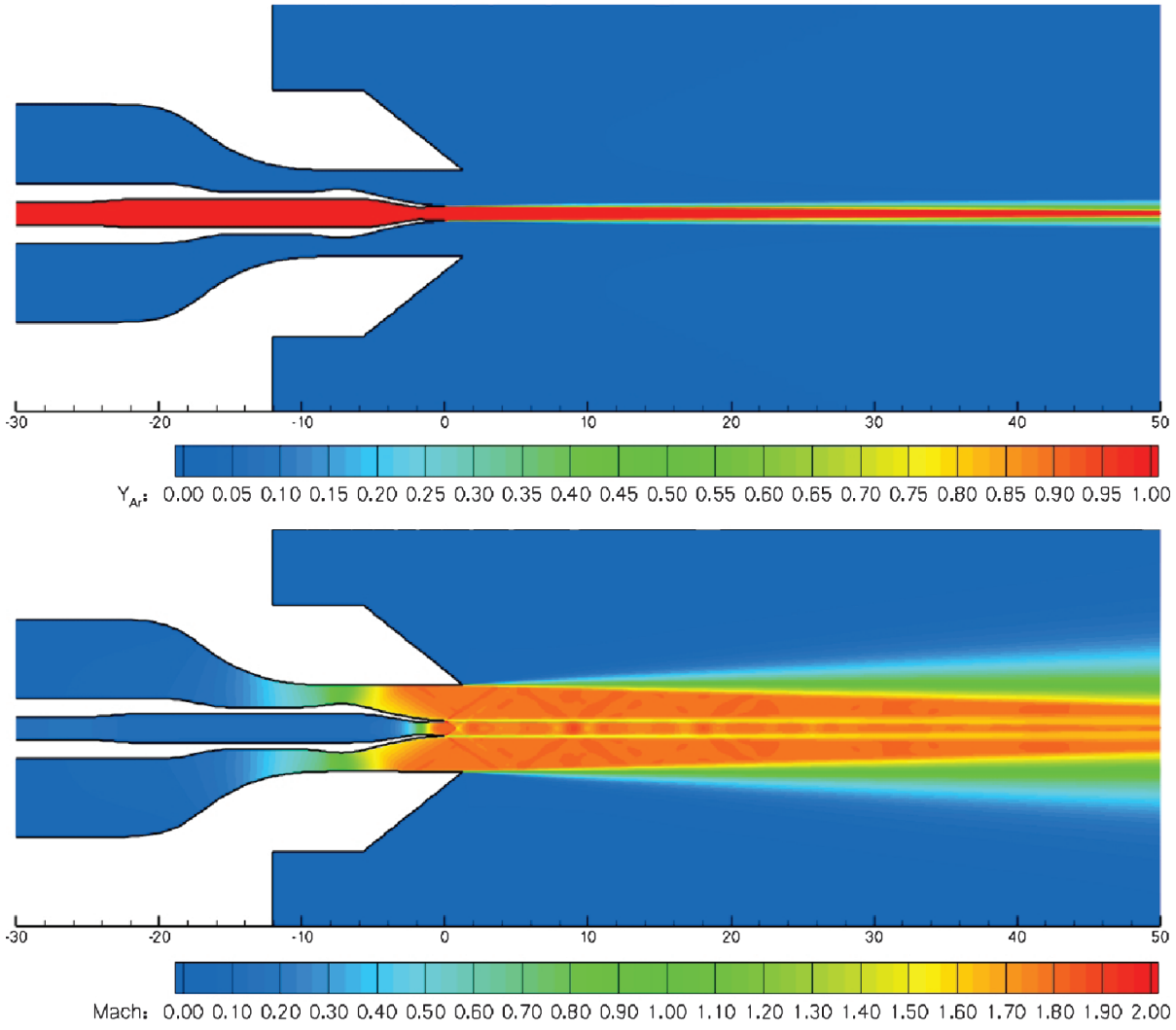

Fig. 8 Contours of argon mass fraction and Mach number for the baseline RAS.

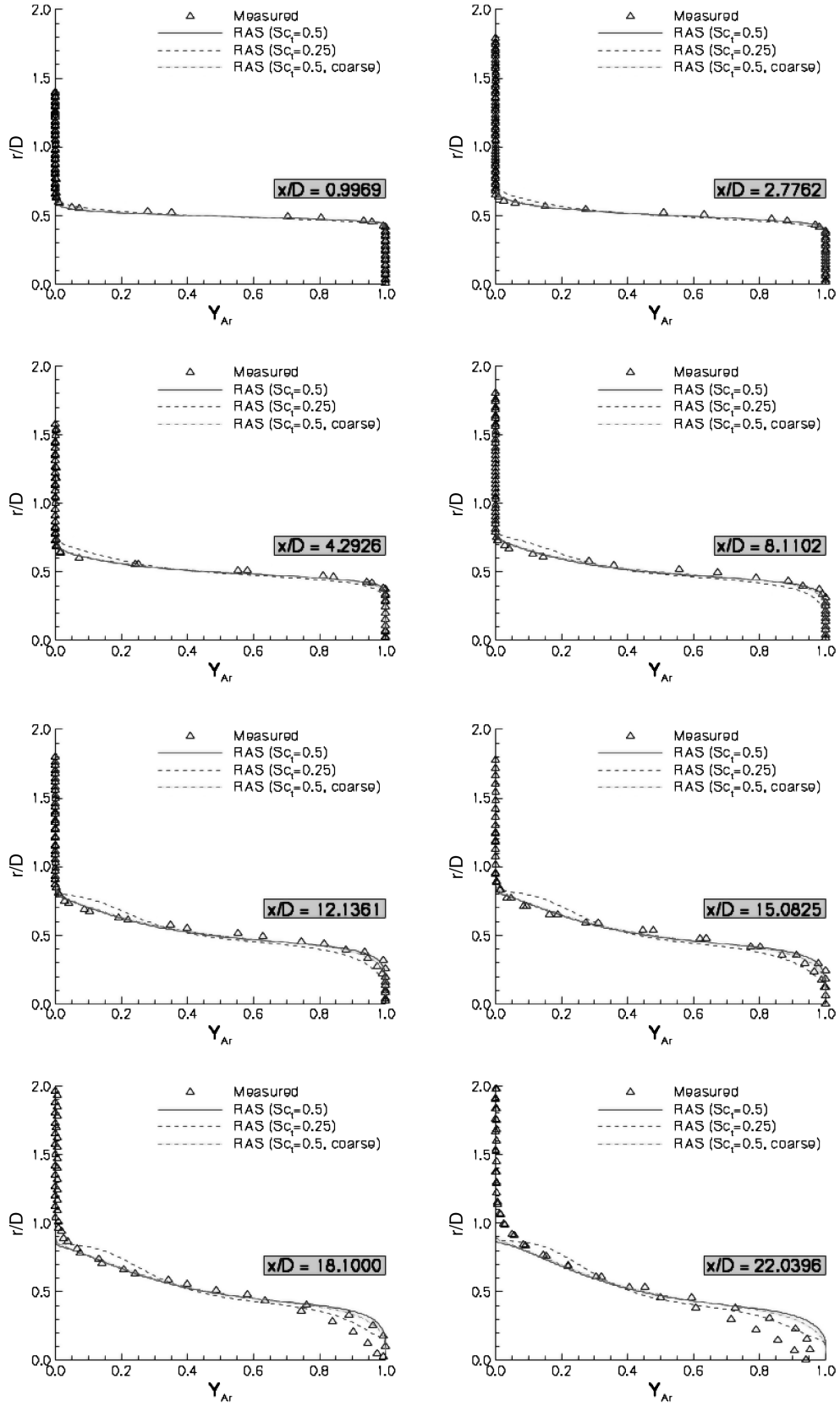

Fig. 9 Comparison of argon mass fraction (RAS predictions) with measured values.

Measured pitot pressure profiles [10] are compared with the RAS results in Fig. 7. The large deficit in pitot pressure near $r/D = 0.5$ is a result of viscous effects from the upstream boundary layers. The small deficit seen near the axis of symmetry at the first four axial stations is a result of the Mach disk formed by the coalescence of the conical shock front that was discussed previously (see Fig. 5). The measured value of this deficit is slightly larger than the predicted value. The pitot pressure deficit is also underpredicted for the coflow shock structure that appears near $r/D = 1.1$ at the first axial station. In general, the best agreement with measurements is given by the $Sc_t = 1.0$ data. The level of agreement seen between this simulation and the measured values is within the measurement uncertainty

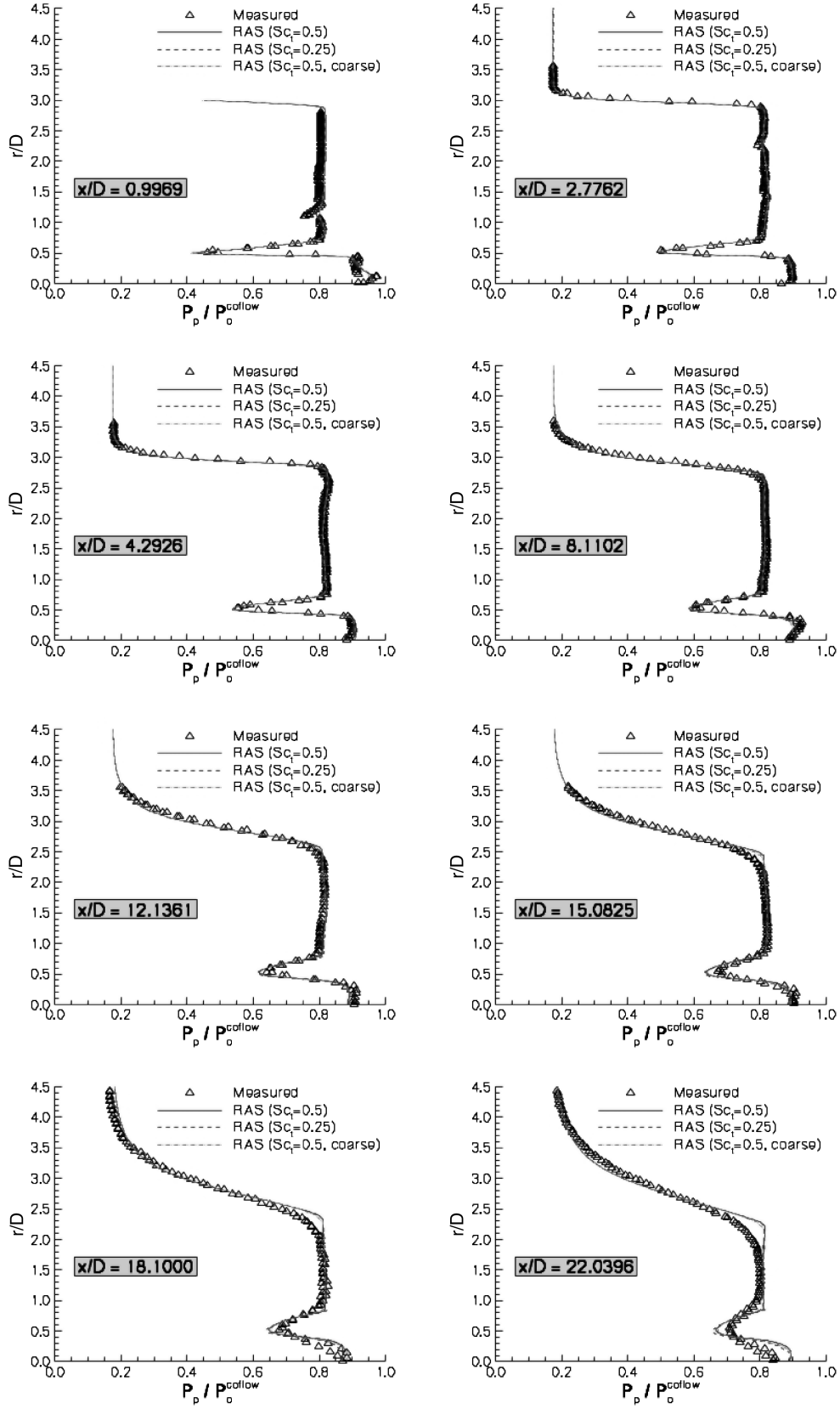

Fig. 10 Comparison of case 2 pitot pressure (RAS predictions) with measured values.

(based solely on the transducer error) of $\pm 0.5\%$ at nearly every measured point for $x/D < 15$. Downstream of this station, the $Sc_t = 1.0$ pitot data underpredict the measured values near the axis and overpredict them near the lower edge of the shear layer present between the coflow jet and the ambient surroundings. Once again, the differences noted between the fine and coarse grid solutions is much smaller than that associated with a modification of the turbulent Schmidt number.

Contours of argon mass fraction and Mach number extracted from the RAS ($Sc_t = 0.5$) are shown in Fig. 8. The argon results show a much longer potential core than that for the helium case. In fact, the potential core in the simulations extends beyond the $x/D = 50$

station, shown in Fig. 8. The slower mixing rate between the two jet streams is a result of the reduced shear associated with case 2. The velocity of the argon stream is only 16% lower than the coflow stream. This is contrasted with the helium case, for which the velocity of the helium stream was more than twice that of the coflow stream. The Mach contours clearly show that the nozzle streams are nearly pressure-matched, and the near-field flow structures are practically identical to those discussed previously for case 1. The far-field shock/expansion pattern is quite different, however, due to the reduced spreading rate of the mixing layer.

Measured argon mass fraction profiles [11] are compared with the RAS results in Fig. 9. The $Sc_t = 0.5$ argon simulation underpredicted the rate of mixing between the coaxial streams. This is in contrast to the helium case, for which the same value of turbulent Schmidt number overpredicted the growth rate of the mixing layer. Hence, an additional simulation was performed with the turbulent Schmidt number reduced by a factor of two. A third simulation was performed (with $Sc_t = 0.5$), using the coarse grid to evaluate the grid dependence. Comparisons are made at the same eight axial stations used to evaluate the helium injection data. The results obtained when reducing the Sc_t value had the desired effect of reducing the length of the potential core of the argon jet. However, this adjustment also resulted in a peculiar inflection point near the outer edge of the mixing layer that was not captured in the measurements. The reduced Schmidt number results also overpredicted the spreading rate of the mixing layer for $x/D < 18$. Overall, the best agreement with measurements was obtained with an Sc_t value of 0.5, which predicted the correct spreading rate of the shear layer for $x/D < 18$. The convective Mach number for the mixing layer was estimated to be 0.16, and so an additional simulation (not shown) was performed with the dilatation–dissipation modification disabled to ensure that the model was not impacting the predictions. As expected, the compressibility correction had no impact on this simulation. One interesting feature noticed in the experimental data is an increased deviation from symmetry that begins to appear at the $x/D = 12$ station. This happens to be the station where the simulations begin to deviate from the measurements. The experimental probes were traversed over the entire coaxial flowfield (i.e., data were gathered for both positive and negative y values relative to the jet axis). Because the data should be axisymmetric in the mean, the measured data were plotted against the absolute value of y in this work, which effectively results in two sets of radial data at each experimental station. The deviation from symmetry is much larger for case 2 than for case 1, which might have implied a slight misalignment of the jet assembly during the argon tests [11]. As was seen for the helium injection conditions, the predictions offered by both the fine and coarse meshes were quite similar.

Measured pitot pressure profiles [11] for case 2 are compared with the RAS results in Fig. 10. The near-field pitot profile features are identical to those seen for case 1, as implied by the Mach contours that were discussed earlier. In general, the level of agreement seen between the simulations and the measured values is within the measurement uncertainty for $x/D < 15$. Downstream of this station, the computed pitot data show sharper features, which are a direct result of the underprediction of the mixing processes at this point in the flowfield. It is interesting to note that the overprediction of the pitot pressure near the lower edge of the shear layer present between the coflow jet and the ambient surroundings ($r/D \approx 2.25$) is larger that what was seen for case 1. The shear between the coflow jet and the ambient environment is practically identical to that for the helium condition. Hence, the underprediction of the argon/air mixing layer has evidently modified the shock system in the outer jet enough to alter the behavior of the coflow/ambient air shear layer.

Hybrid Reynolds-Averaged/Large-Eddy Simulation Results

The coaxial flowfields examined in this effort have three distinct flow regions: center jet, coflow jet, and the ambient surroundings. The core velocity in the coflow jet was 480 m/s, and the center jet values were 1100 (helium) and 400 m/s (argon). The ambient air region was almost stagnant. This presented a problem, in that the hybrid RAS/LES approach requires a time-accurate integration with a time step small enough to temporally resolve turbulent structures at scales representative of a computational cell width. A time step appropriate for resolving a turbulent structure in the jet flow is given by the following estimate:

$$\Delta t \approx \frac{\Delta x}{\max(u_{\text{inj}}, u_{\text{air}})} \tag{5}$$

Based on the disparate characteristic velocities between the jet flows and the ambient air, this definition would require hundreds of time steps to transport a particle across one cell length in the ambient air region. Fortunately, the shear layer of interest is the mixing layer between the supersonic jets rather than the shear layer present between the coflow jet and the ambient air. Hence, the time scale dilemma was dealt with by forcing the hybrid RAS/LES model to remain in RAS mode for the outer portion of the coflow jet and the ambient region. In particular, an initial solution was obtained for the entire flowfield using a steady-state RAS. The calculation was then restarted using the hybrid RAS/LES approach with the blending function forced to unity for $r/D > 2$. This value was found to be large enough to contain all convecting coherent structures formed in the mixing layer between the two jet flows for the LES domain of interest.

The form of SGS closure used in this effort was based on the one-equation formulation of Yoshizawa and Horiuti [21]. The Yoshizawa model involves an evolution equation for the SGS turbulence kinetic energy:

$$\frac{\partial}{\partial t}(\rho k) + \frac{\partial}{\partial x_j}(\rho k u_j) = \frac{\partial}{\partial x_j}\left[(\mu + \mu_t)\frac{\partial k}{\partial x_j}\right] + P_k - C_d \rho \frac{k^{(3/2)}}{\Delta} \tag{6}$$

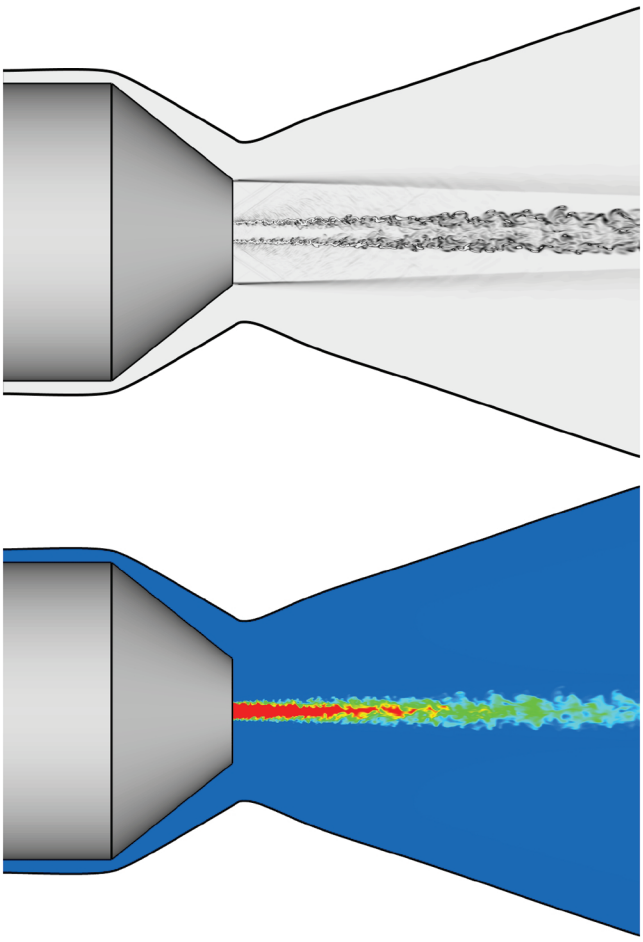

Fig. 11 Instantaneous Schlieren and normalized helium mass fraction contours (hybrid RAS/LES).

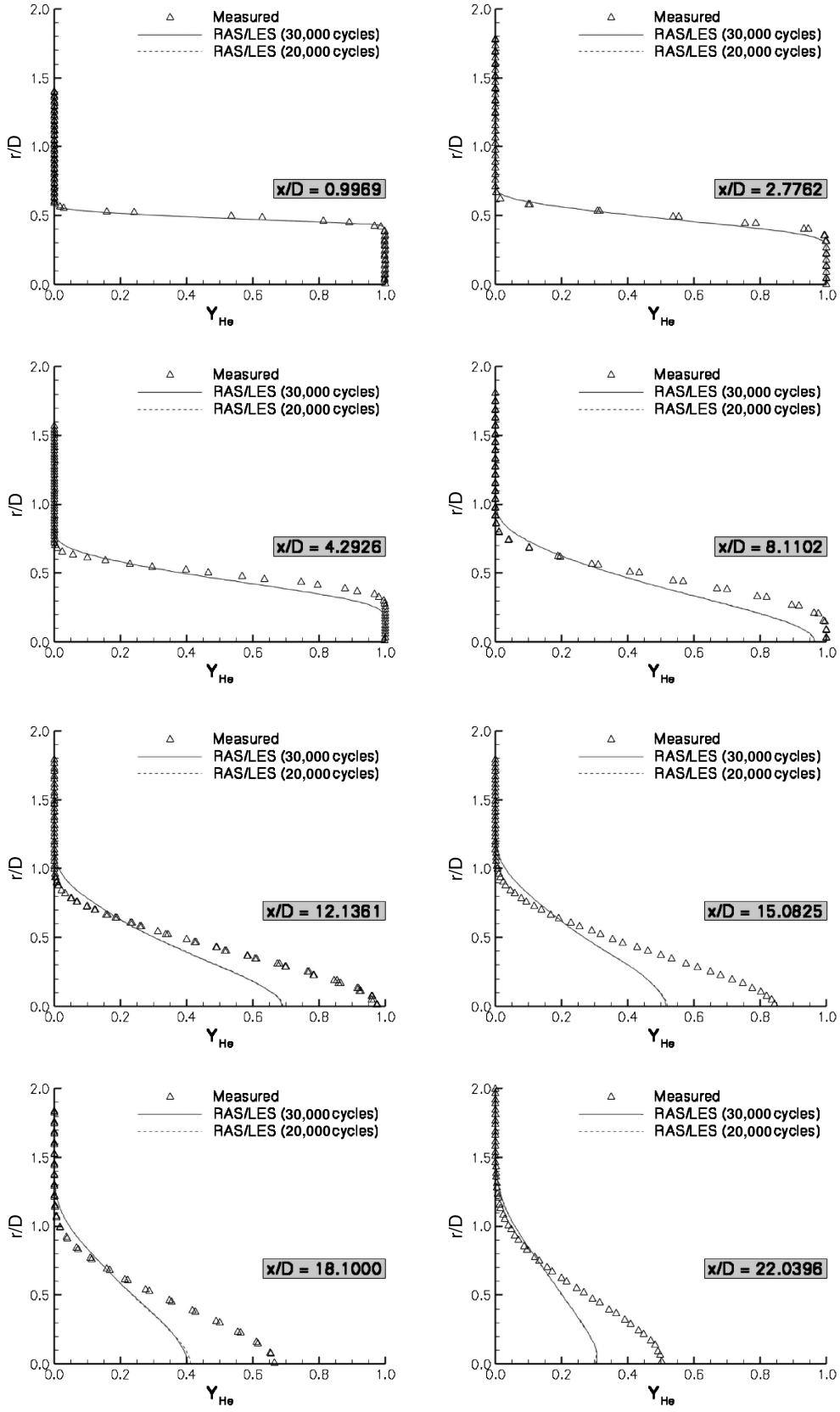

Fig. 12 Comparison of normalized helium mass fraction (averaged hybrid RAS/LES predictions) with measured values.

where

$$P_k = \left[\mu_t\left(\frac{\partial u_i}{\partial x_j}+\frac{\partial u_j}{\partial x_i}\right)-\frac{2}{3}\delta_{ij}\left(\rho k+\mu_t\frac{\partial u_k}{\partial x_k}\right)\right]\frac{\partial u_i}{\partial x_j} \tag{7a}$$

$$\mu_t = C_\mu \rho k^{\frac{1}{2}}\Delta \tag{7b}$$

However, two noteworthy modifications to the model were made for this effort. The first modification involves the definition of the filter width Δ. Traditional LES practitioners have tended to work with truly isotropic grids, justifying the use of a simple isotropic definition for the filter width (e.g., the cubed root of the cell volume). Grids used for configurations of engineering interest, however, will have some

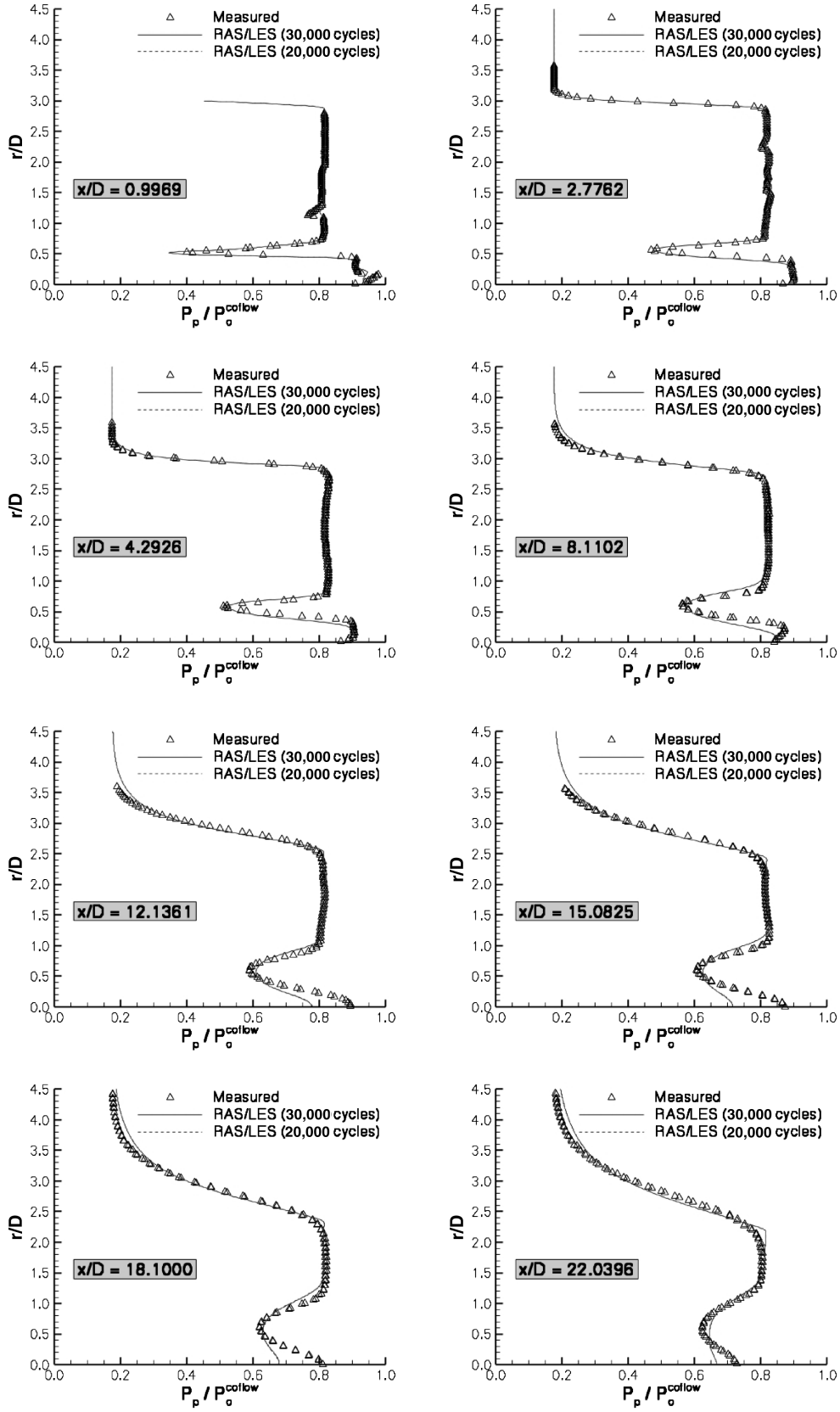

Fig. 13 Comparison of case 1 pitot pressure (averaged hybrid RAS/LES predictions) with measured values.

level of anisotropy. Hence, hybrid RAS/LES practitioners tend to prefer the following anisotropic definition for the filter width:

$$\Delta = \max(\Delta_i, \Delta_j, \Delta_k) \tag{8}$$

In this expression, Δ_i, Δ_j, and Δ_k denote the width along each computational direction of a 3-D hexahedral grid cell. The second modification affects the level of SGS viscosity in LES regions. At equilibrium [defined when production balances dissipation in Eq. (6)], the Yoshizawa model reduces to an algebraic Smagorinsky closure model. The effective Smagorinsky constant C_s implied by the model under equilibrium conditions is given by the following expression:

$$(C_s)^2 = \sqrt{2}C_\mu \left(\frac{C_\mu}{C_d}\right)^{(1/2)} \tag{9}$$

The default values given in [21] for C_μ and C_d are 0.05 and 1.0, respectively. The value of C_s implied by these values is 0.126. There is no universal value for this Smagorinsky constant, but the LES community has typically endorsed values on the order of 0.2 for homogeneous turbulence and 0.065 for shear flows [26]. Initial calculations used a reduced value of 0.02075 for C_μ to recover the accepted Smagorinsky constant for shear flows. This value, however, resulted in a solution with an excessive delay in the formation of resolved turbulent structures. The numerical dissipation of the second-order upwind numerical framework used in this effort is on the same order as the SGS viscosity Δ^2; hence, one might expect lower levels of SGS viscosity to be required. A value of $C_\mu = 0.00823$ was found to readily unlock significant levels of resolved turbulence energy in the present simulations. This value enforces a Smagorinsky constant of 0.0325 (half the recommended value for shear flows) under equilibrium conditions, and it was selected as the baseline setting.

An instantaneous snapshot of the flowfield for case 1 is shown in Fig. 11. The top image displays the density gradient magnitude (numerical approximation of a Schlieren image) to illustrate the flow structure, and the bottom image shows the normalized helium mass fraction contours. A significant level of resolved turbulent content was captured in the simulation. The recirculation zone behind the base of the centerbody provided a source of large-scale unsteadiness that rapidly triggered Kelvin–Helmholtz instabilities in the shear layer. These instabilities transitioned the flow from a fully modeled Reynolds-averaged state exiting the nozzle to a primarily resolved turbulent state a few jet diameters downstream of the nozzle exit plane. Unsteady shock and expansion waves are seen reflecting through the jet structure. The shear layer between the outer jet and ambient air maintained the desired steady-state Reynolds-averaged behavior, due to the forced usage of the RAS equations outside of $r/D = 2.0$. The high level of shear associated with this operating condition provided a strong mechanism for turbulence production, as illustrated by the rich array of vortical structures seen in the helium contours. These structures provide the turbulent stirring that leads to enhanced mixing by stretching the interface between the air and injectant.

Before gathering any statistics, time integrations were performed for two complete flow-through times to flush out the initial transients during the transition from the converged RAS solution to the hybrid RAS/LES result. This relatively small time interval was sufficient due to a lack of any large regions of separated flow and the fact that the ambient region was essentially frozen in its Reynolds-averaged state. At this point, running averages were computed and stored after each time step. To reduce the integration time required to gather meaningful statistics, a combination of temporal and spatial (in the circumferential direction) averaging was performed. The spatial average was made possible by a three-step process. The first step was to interpolate the ensemble-averaged data onto a polar grid topology (in the crossflow plane) at the experimental streamwise stations. The second step involved a coordinate transformation of the flow data to a cylindrical coordinate system (x, y, $z \rightarrow x$, r, θ). The final step was to average the transformed variables along the azimuthal curves of constant radius (which corresponds to the spatially homogeneous direction). All three steps were performed using the Tecplot post-processing package [27] and automated using the Tecplot macro-scripting language.

The averaged hybrid RAS/LES helium mass fraction profiles are compared with the measurements in Fig. 12. In general, the predictions show a shear layer growth rate that is more rapid than that implied by the measurements. As mentioned previously, the SGS model coefficients were adjusted to promote the onset of flow instabilities. It appears that this adjustment leads to an inappropriate level of modeled viscosity (i.e., a value that is too low) once the Kelvin–Helmholtz instabilities have transitioned to a fully turbulent state. This situation might be improved if resolved turbulent structures were present at the nozzle exit plane. This would alleviate the delay in transition that is associated with the conversion of modeled Reynolds-averaged turbulence to resolved LES content, and it would allow a larger Smagorinsky coefficient to be used. One reasonably economic approach to this task is to implement recycling/rescaling techniques [28–30]. This will be the focus of future efforts. A comparison of the averaged hybrid RAS/LES results with those obtained using pure RAS at the default ($Sc_t = 0.5$) condition show many similarities. This particular RAS simulation also overpredicted the shear layer growth rate, but one noteworthy difference between the results is the manner in which the helium mass fraction asymptotically approaches zero at the edge of the mixing layer. RAS approaches are notorious for producing a sharp nonphysical interface at the edge of the shear layer. The hybrid RAS/LES results show a much smoother asymptotic decay that is more representative of the measurements. Statistical convergence has been assessed by comparing the statistics extracted over successively larger time-step intervals. The statistics extracted over 20,000 and 30,000 time steps (cycles) show practically identical results. Another useful statistical convergence check is to examine the averaged azimuthal velocity component. This value should approach zero as the statistics are converged. The maximum absolute value of azimuthal velocity (averaged over 30,000 cycles) was 2.5 m/s, or roughly 0.2% of the peak streamwise velocity.

The averaged pitot pressure profiles are compared with the measurements in Fig. 13. These results reinforce the assertion that the mixing layer growth rate has been overpredicted, particularly at stations downstream of an x/D of four. Although the deficit in the pitot pressure profile is broader across the shear layer, the qualitative features of the profile shape mimics that of the measurements. This was not the case in the RAS results that overpredicted the level of

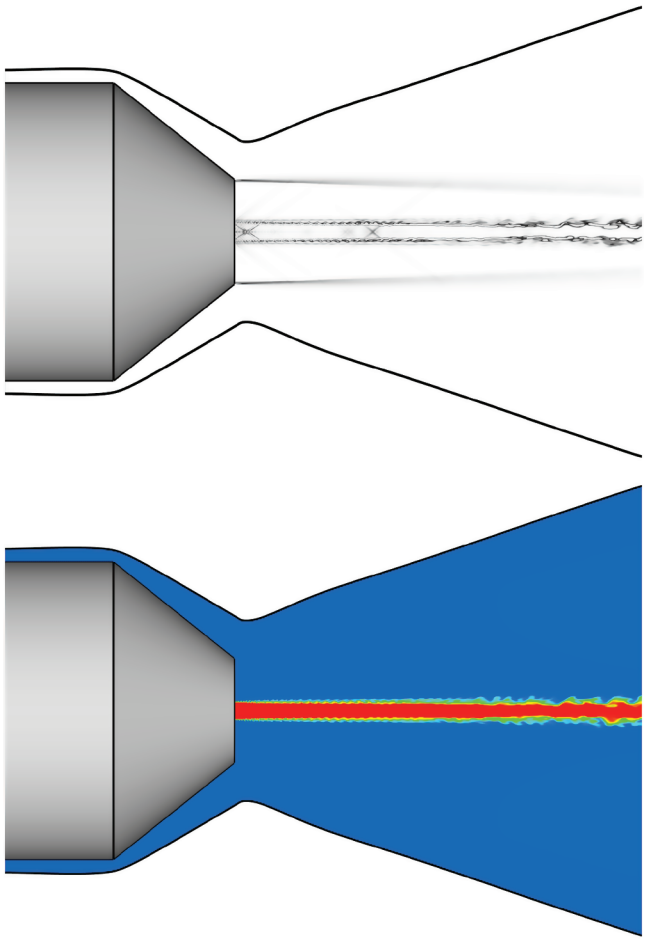

Fig. 14 Instantaneous Schlieren and argon mass fraction contours (hybrid RAS/LES).

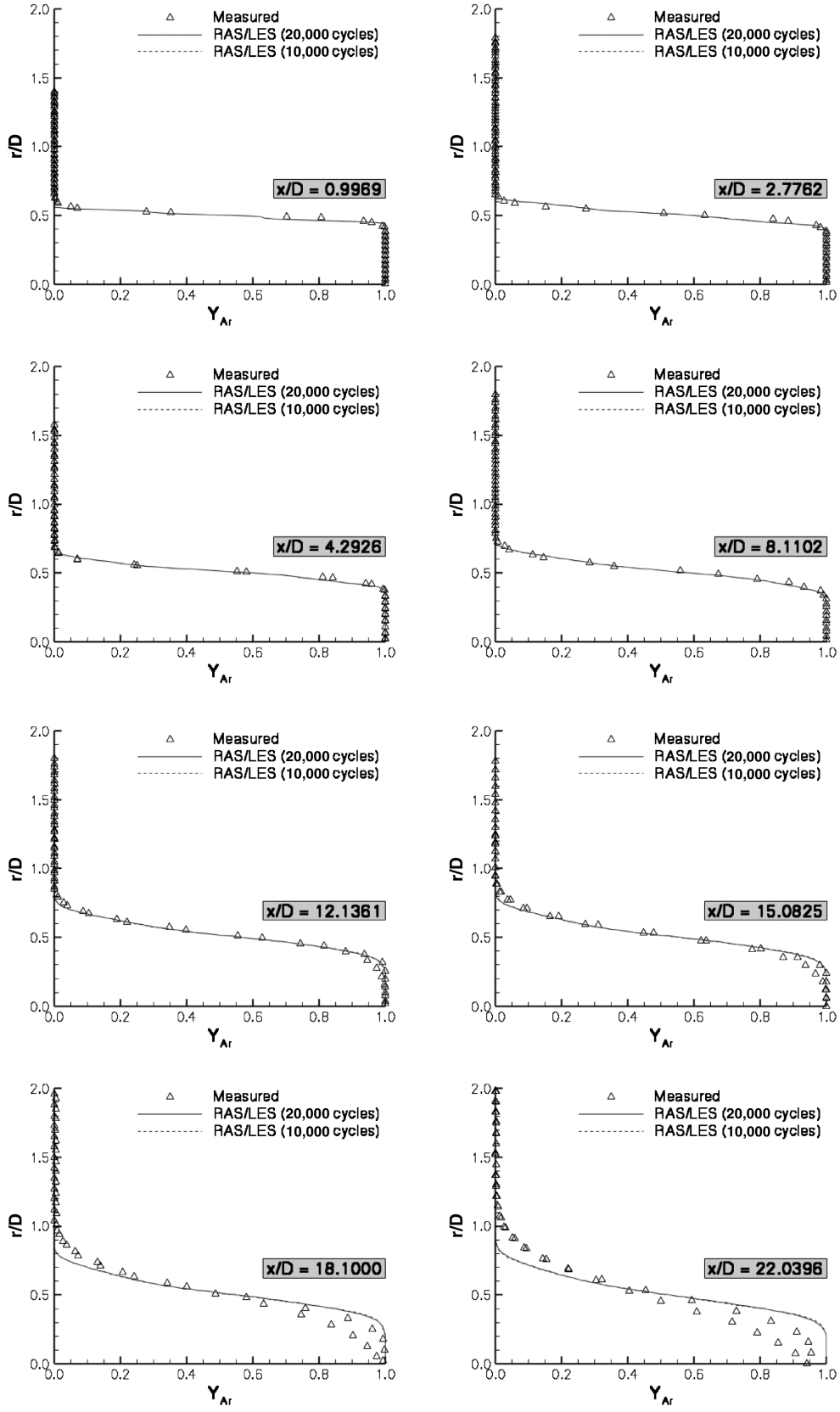

Fig. 15 Comparison of argon mass fraction (averaged hybrid RAS/LES predictions) with measured values.

mixing. The finer details of the flow structure (e.g., the slight pressure deficit due to the Mach disk at the axis) are also evident in the hybrid RAS/LES data. As was the case with the helium mass fraction statistics, the averaged pitot pressure profiles for both averaging intervals show practically identical results, suggesting that the first-order moments are well converged.

An instantaneous snapshot of the flowfield for case 2 is shown in Fig. 14. The top image displays a numerical Schlieren of the flow structure, whereas the lower image displays the argon mass fraction distribution. The Kelvin–Helmholtz instabilities are clearly visible in both images and persist for many jet diameters before breaking down into fully 3-D turbulent structures. This transition process begins

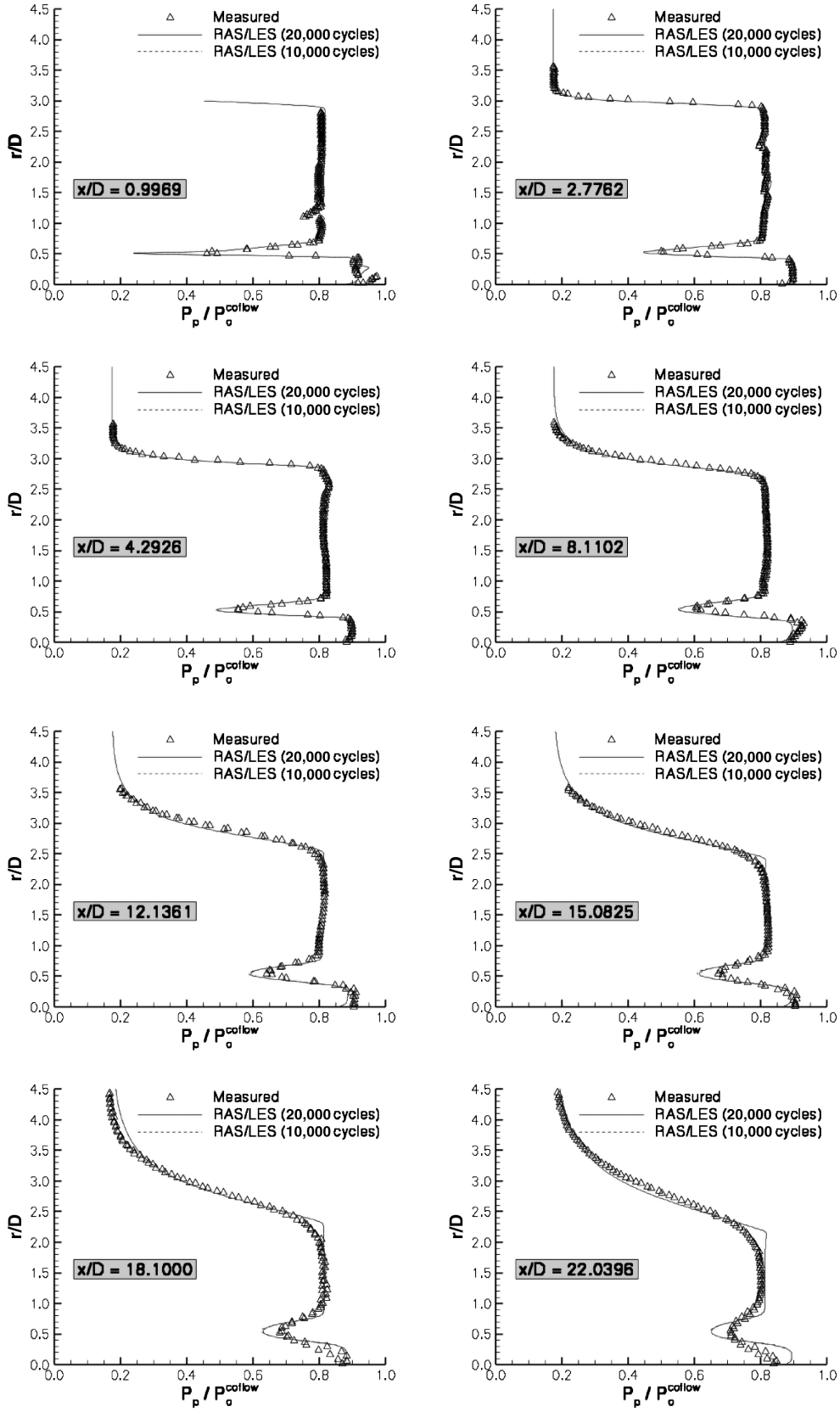

Fig. 16 Comparison of case 2 pitot pressure (averaged hybrid RAS/LES predictions) with measured values.

near an x/D of 10 or 12, in which the last visible wave structures appear in the Schlieren image. The low level of shear for this case (as compared with case 1) is the root cause for the delay in the breakdown of the Kelvin–Helmholtz instabilities. These instabilities are also primarily two-dimensional in nature: an expected result given the low convective Mach number of this mixing layer. Large (i.e., on the order of the jet diameter) turbulent coherent structures do not appear until an x/D of 15 to 20. Hence, the turbulent stirring processes that lead to enhanced mixing are not prevalent until the latter stages of the LES domain.

The averaged hybrid RAS/LES argon mass fraction profiles are compared with measurements in Fig. 15. Overall, the level of

turbulent mixing between the argon and air jets was underpredicted. These results are comparable with those obtained using the RAS approach (see Fig. 9), although the hybrid RAS/LES shows a slightly reduced mixing level at the last experimental station. The smooth asymptotic transition of the argon profile toward zero at the edge of the mixing layer is again captured in the hybrid RAS/LES results. The reduced spreading rate of the shear layer is also seen in the pitot pressure profile comparisons displayed in Fig. 16. The peak shear layer deficit is consistently overpredicted at each station. Future work will examine the influence of providing realistic resolved turbulent content at the exit of the coaxial nozzles. This may be particularly important for the present application, because the boundary layer thickness of the approach coflow is an order of magnitude thicker than the blunt base region that is currently triggering the unsteadiness. The statistics gathered after 10,000 cycles show practically identical results as the data averaged over 20,000 cycles, suggesting that the statistics are converged for these first-order correlations. The maximum azimuthal velocity (averaged over 20,000 cycles) was 0.6 m/s, or roughly 0.1% of the peak streamwise velocity.

Second-Order Correlations

The primary second-order correlations that are modeled in the RAS equation set are the Reynolds stress tensor and the Reynolds heat and mass flux vectors. The Reynolds stress tensor is typically modeled by the Boussinesq approximation:

$$\overline{\rho u_i'' u_j''} = \frac{2}{3}\delta_{ij}\left(\rho k + \mu_t \frac{\partial u_k}{\partial x_k}\right) - \mu_t\left(\frac{\partial u_i}{\partial x_j} + \frac{\partial u_j}{\partial x_i}\right) \tag{10}$$

and the Reynolds flux vectors commonly use gradient diffusion models; that is,

$$\overline{\rho h'' u_j''} = -\frac{\mu_t}{Pr_t}\frac{\partial h}{\partial x_j} \tag{11}$$

and

$$\overline{\rho Y_m'' u_j''} = -\frac{\mu_t}{Sc_t}\frac{\partial Y_m}{\partial x_j} \tag{12}$$

The accuracy of the modeling employed for these terms is critical for the success of RAS approaches. Measured data for each of the previous correlations are scarce, and so it is often difficult to directly assess the accuracy of the RAS closures. One of the primary goals of this effort was to use the hybrid RAS/LES simulations to assess the performance of the RAS modeling. Ideally, one would hope for a close match between the hybrid RAS/LES results and available measurements, but the level of agreement obtained in this effort was not entirely satisfying. Nevertheless, some insight into the RAS modeling can be gleaned by comparing the modeled terms with the values extracted from the resolved LES field.

The rms of the streamwise velocity fluctuation is considered first. This quantity was the only second-order correlation that was measured, and the measurement was only taken for case 1. These measurements were made using the RELIEF [12] oxygen flow tagging technique. Figure 17 compares the measured values with the values computed from the RAS ($Sc_t = 0.5$) result using Eq. (10), as well as the ensemble averages extracted from the hybrid RAS/LES. The modeled RAS values agree remarkably well with the measurements in the early stages of the shear layer development, but the width of the profile is underpredicted at stations further downstream. The hybrid RAS/LES results overpredict the rms values in the shear layer at the first station, but the profiles at the stations further downstream compare favorably with the measurements. One particularly noteworthy feature is the buildup of turbulent fluctuations in the core flow near the axis that is present in the hybrid RAS/LES results. This feature is absent from the RAS result, because the mean flow gradients are relatively small outside of the shear layer. Mean velocity gradients are the sole source of turbulence production for most RAS models. The enforcement of a RAS behavior for $r/D > 2$ in the hybrid RAS/LES simulations prevented the formation of unsteady turbulence structures in the outer jet/ambient air shear layer: limiting the buildup of rms velocity levels in the core of the outer jet. Hence, the core flow values in the outer jet, although larger than that predicted by pure RAS, were underpredicted.

The rms radial and azimuthal velocity fluctuations are compared in Figs. 18 and 19. Linear eddy viscosity models based on the Boussinesq approximation tend to produce nearly isotropic velocity

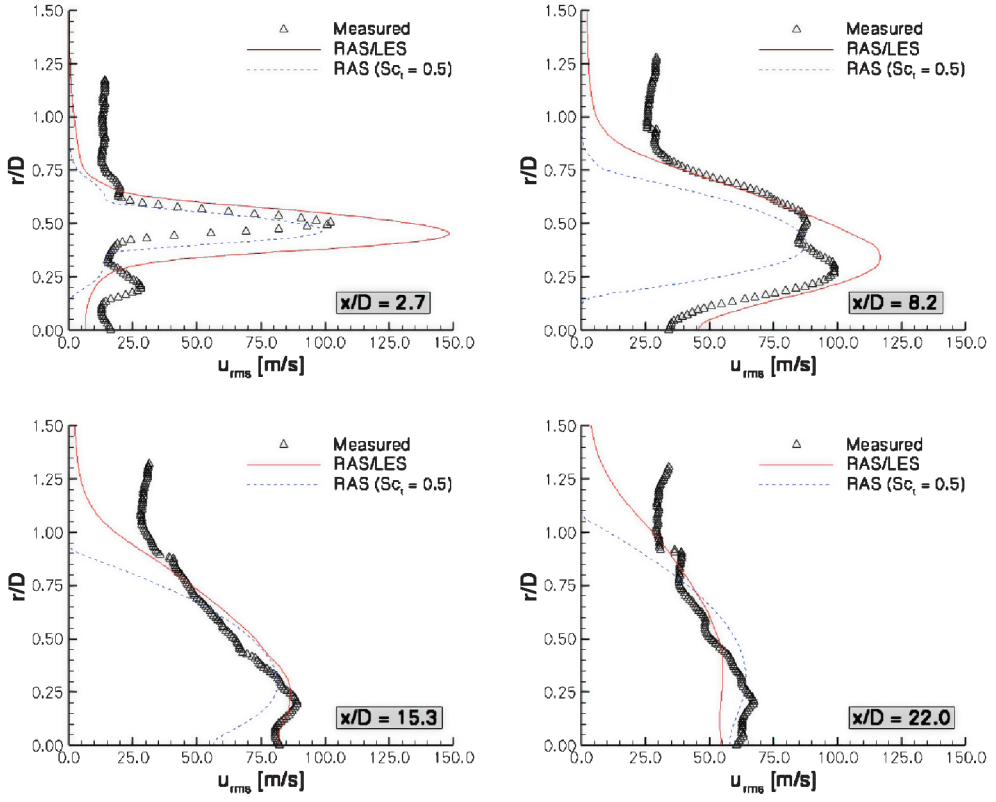

Fig. 17 Comparison of case 1 streamwise velocity fluctuation rms with measured values.

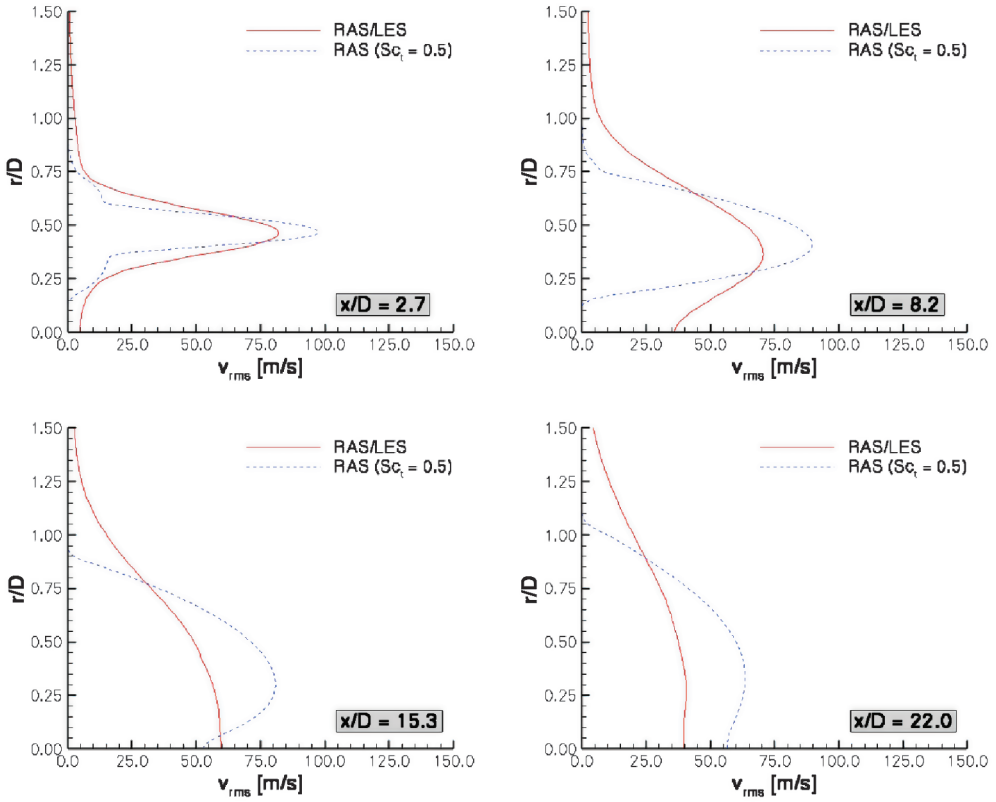

Fig. 18 Comparison of case 1 radial velocity fluctuation rms.

variances (normal stresses) when applied to strain dominated flows. The degree of anisotropy is governed by the magnitude of the velocity gradients (other than those contributing to the strain rate) relative to the $\frac{2}{3}\rho k$ term, as shown by Eq. (10). Hence, it is not surprising that the RAS model returned a nearly isotropic set of normal stresses for this turbulent shear flow. The hybrid RAS/LES data, on the other hand, showed a nonnegligible level of anisotropy in the velocity variances. In particular, the streamwise velocity variance was substantially larger than the crossflow variances. This result is typical for shear dominated flows.

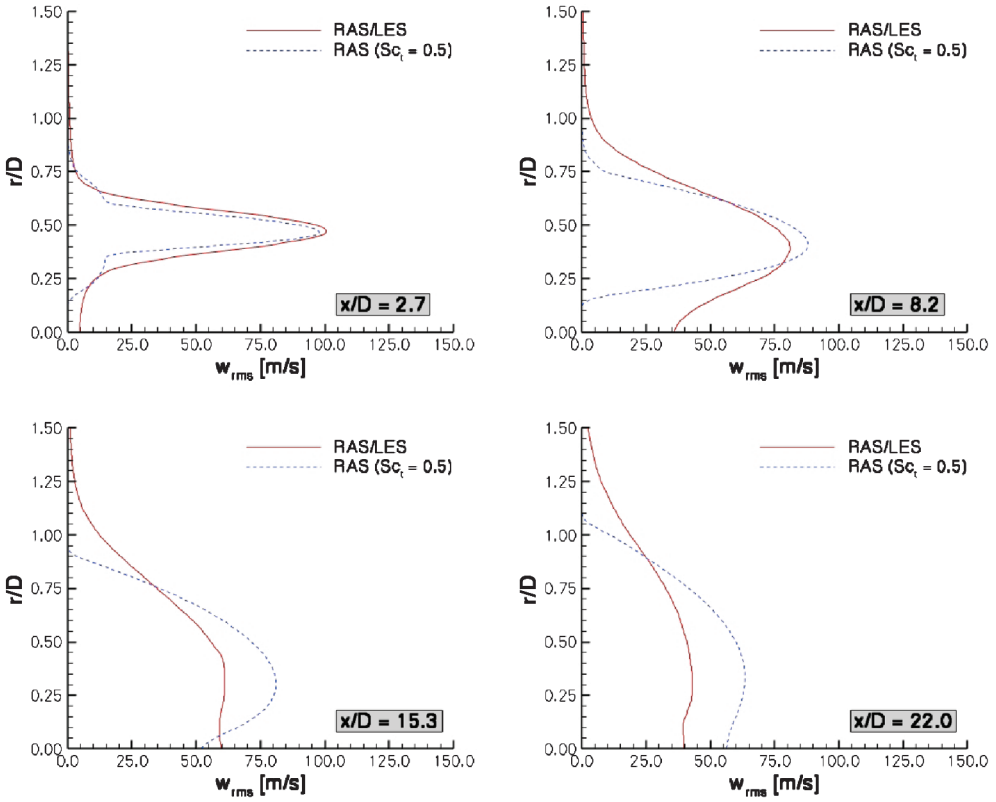

Fig. 19 Comparison of case 1 azimuthal velocity fluctuation rms.

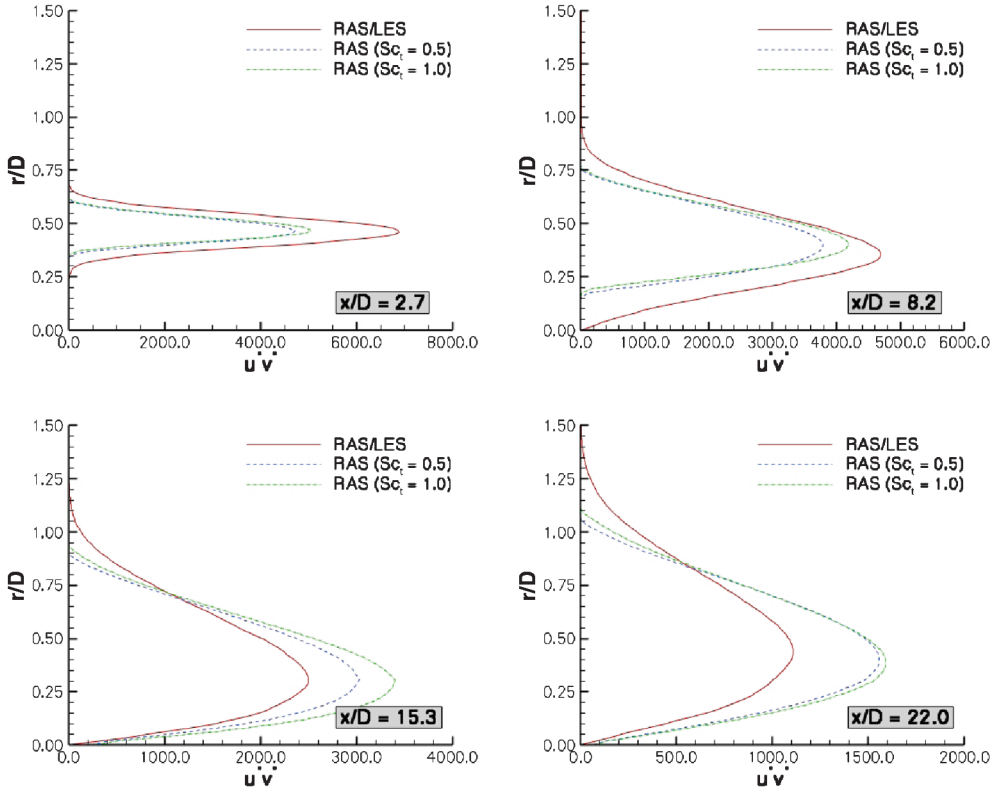

Fig. 20 Comparison of case 1 $\widetilde{u''v''}$ (Reynolds shear stress correlation).

The Reynolds shear stress ($\widetilde{u''v''}$) and the Reynolds mass flux $\widetilde{Y''_{\mathrm{He}}v''}$ terms are compared in Figs. 20 and 21. The accuracy of the RAS equations, to a large extent, is driven by how well these terms are modeled. Because the $Sc_t = 1.0$ RAS data compared favorably to the measured mean flow properties, correlations computed from this simulation were also added to the figures. The shear stress extracted from the hybrid RAS/LES data is larger than those produced by the RAS models at the first two axial stations. The situation is reversed at the last two stations. This result is consistent with the fact that the hybrid RAS/LES results predicted a more rapid mixing rate than the RAS approaches. A similar behavior is evident in the Reynolds mass flux vector. The hybrid RAS/LES data showed the most rapid

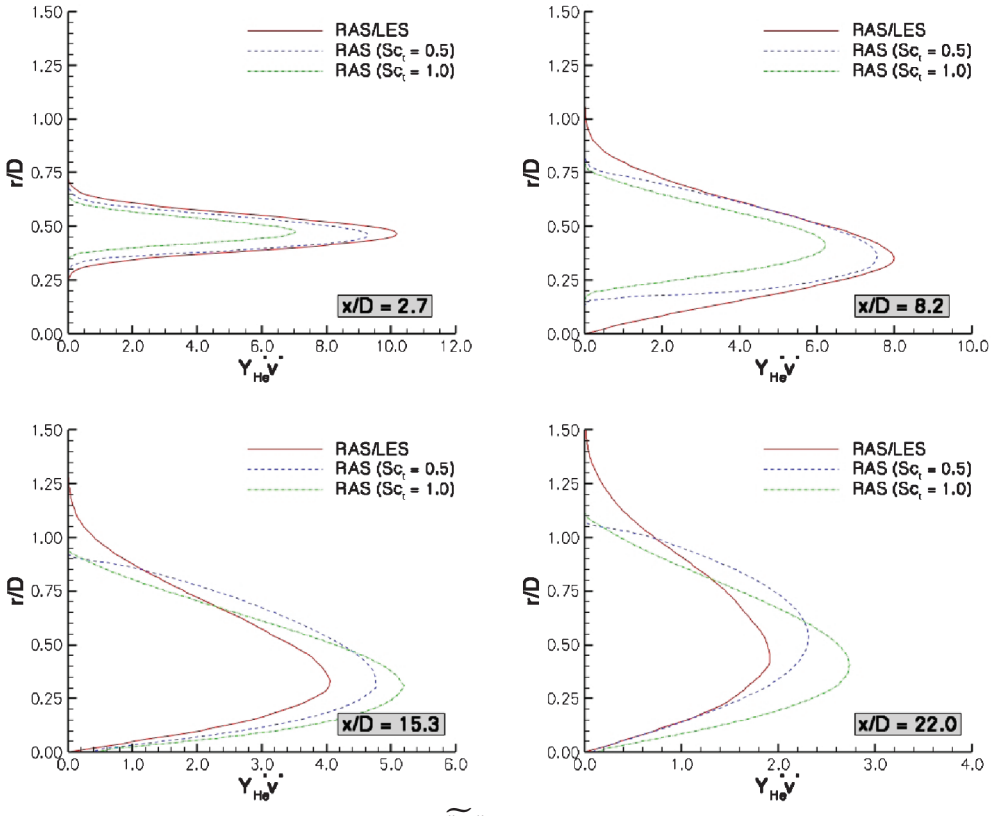

Fig. 21 Comparison of $\widetilde{Y''_{\mathrm{He}}v''}$ (Reynolds mass flux correlation).

mixing, the $Sc_t = 1.0$ RAS yielded the slowest mixing rate, and the $Sc_t = 0.5$ RAS result was somewhere in between. Hence, at the early axial stations, the turbulent mixing rate should be largest for the hybrid RAS/LES and smallest for the $Sc_t = 1.0$ RAS. Once the mixing process has reached some critical level, the mixing rate will begin to decay. Thus, at some station downstream, the rate of mixing extracted from a simulation with a slower mixing rate will eventually exceed the rate extracted from a simulation with a more rapid mixing rate. This is precisely the situation that occurs between the second and third streamwise stations shown in Fig. 21.

Conclusions

Reynolds-averaged and hybrid Reynolds-averaged and large-eddy simulations have been performed to model a supersonic coaxial jet flow experiment. The experiment consists of an outer jet of air and an inner jet that was either a helium–oxygen mixture or pure argon. Both jets exhausted into an ambient environment. The Mach 1.8 nozzle flows exiting the test apparatus were nearly pressure-matched for both injectant conditions. However, the level of shear and the compressibility of the mixing layer varied, depending on the injectants involved. The helium condition resulted in a highly compressible mixing layer with a convective Mach number of 0.7. The argon condition, on the other hand, was nearly velocity-matched and produced a mixing layer with a convective Mach number of 0.16. A comprehensive set of measurements were taken, which included pitot pressure, mean and rms velocities, and gas sampling. The model geometry, flow conditions, and measurement uncertainties were all well documented, resulting in a package that was well suited for model validation efforts.

The goal of the computational effort was to assess the state of the art for both RAS and hybrid RAS/LES approaches, as applied to compressible turbulent flows. The Reynolds-averaged simulation for the helium cases displayed a strong sensitivity to choice of turbulent Schmidt number. A value of 1.0 was found to be an optimal choice for this flow condition. However, a lower turbulent Schmidt number, on the order of 0.5, provided the best match with measurements for the argon case. The uncertainty involved with appropriate choices for RAS modeling parameters highlights the difficulty with using these approaches for predictive simulations. In principle, LES or hybrid RAS/LES methods have the potential to reduce this uncertainty by resolving a substantial fraction of the turbulent flowfield. The hybrid simulations performed in this effort, however, were no more predictive than the baseline Reynolds-averaged predictions. The explanation provided for the discrepancy between the hybrid RAS/LES results and the measurements centered around issues related to how the Reynolds-averaged state transitions to a state with resolved turbulent content. The addition of resolved turbulent content to the inflow conditions was suggested to address this concern. Finally, comparisons made between resolved second-order turbulence statistics and their modeled Reynolds-averaged counterparts were discussed. Refined hybrid simulations are required, however, to improve the accuracy of the hybrid RAS/LES results before any solid conclusions can be drawn concerning the RAS modeling.

Acknowledgments

The research was supported by the Hypersonics Project of the NASA Fundamental Aerodynamics Program. This effort was performed by the Hypersonic Airbreathing Propulsion Branch at the NASA Langley Research Center.

References

[1] Baurle, R. A., and Eklund, D. R., "Analysis of Dual-Mode Hydrocarbon Scramjet Operation at Mach 4–6.5," *Journal of Propulsion and Power*, Vol. 18, No. 5, Sept.–Oct. 2002, pp. 990–1002. doi:10.2514/2.6047

[2] Eklund, D. R., Baurle, R. A., and Gruber, M. R., "Computational Study of a Supersonic Combustor Fueled by an Aerodynamic Ramp Injector," AIAA Paper 2001-0379, Jan. 2001.

[3] Rodriguez, C. G., and Cutler, A. D., "Computational Simulations of a Supersonic-Combustion Benchmark Experiment," AIAA Paper 2004-4424, July 2004.

[4] Spalart, P. R., Jou, W.-H., Strelets, M., and Allmaras, S. R., "Comments on the Feasibility of LES for Wings, and on a Hybrid RANS/LES Approach," *Advances in DNS/LES*, edited by C. Liu, and Z. Liu, Greyden Press, Columbus, OH, Aug. 1997, p. 137.

[5] Speziale, C. G., "Turbulence Modeling for Time Dependent RANS and VLES: A Review," *AIAA Journal*, Vol. 36, No. 2, 1998, pp. 173–184. doi:10.2514/2.7499

[6] Baurle, R. A., Tam, C.-J., Edwards, J. R., and Hassan, H. A., "Hybrid Simulation Approach for Cavity Flows: Blending, Algorithm, and Boundary Treatment Issues," *AIAA Journal*, Vol. 41, No. 8, Aug. 2003, pp. 1463–1480. doi:10.2514/2.2129

[7] Menter, F. R., and Kuntz, M., "Adaptation of Eddy-Viscosity Turbulence Models to Unsteady Separated Flow Behind Vehicles," *The Aerodynamics of Heavy Vehicles: Trucks, Buses, and Trains.*, edited by R. McCallen, F. Browand, and J. Ross, Springer Berlin, 2002.

[8] Spalart, P. R., Deck, S., Shur, M. L., Squires, K. D., Strelets, M., and Travin, A., "A New Version of Detached-Eddy Simulation, Resistant to Ambiguous Grid Densities," *Theoretical and Computational Fluid Dynamics*, Vol. 20, No. 3, 2006, pp. 181–195. doi:10.1007/s00162-006-0015-0.

[9] Girimaji, S. S., "Partially-Averaged Navier-Stokes Model for Turbulence: A Reynolds-Averaged Navier-Stokes to Direct Numerical Simulation Bridging Method," *Journal of Applied Mechanics*, Vol. 73, No. 3, 2006, pp. 413–421. doi:10.1115/1.2151207

[10] Cutler, A. D., Diskin, G. S., Drummond, J. P., and White, J. A., "Supersonic Coaxial Jet Experiment for Computational Fluid Dynamics Code Validation," *AIAA Journal*, Vol. 44, No. 3, March 2006, pp. 585–592. doi:10.2514/1.5781

[11] Clifton, C. W., and Cutler, A. D., "A Supersonic Argon/Air Coaxial Jet Experiment for Computational Fluid Dynamics Code Validation," NASA CR 214866, April 2007.

[12] Miles, R. B., Grinstead, J., Kohl, R. H., and Diskin, G. S., "The RELIEF Flow Tagging Technique and its Application in Engine Testing Facilities and for Helium–Air Mixing Studies," *Measurement Science and Technology*, Vol. 11, No. 9, 2000, pp. 1272–1281. doi:10.1088/0957-0233/11/9/304.

[13] Papamoschou, D., and Roshko, A., "The Compressible Turbulent Shear Layer: An Experimental Study," *Journal of Fluid Mechanics*, Vol. 197, Dec. 1988, pp. 453–477. doi:10.1017/S0022112088003325

[14] White, J. A., and Morisson, J. H., "Pseudo-Temporal Multi-Grid Relaxation Scheme for Solving the Parabolized Navier–Stokes Equations," AIAA Paper 99-3360, June 1999.

[15] VULCAN, Ver. 6.0.2., http://vulcan-cfd.larc.nasa.gov/, NASA Langley Research Center, Hampton, VA, Jan. 2007.

[16] Edwards, J. R., "A Low Diffusion Flux-Splitting Scheme for Navier-Stokes Calculations," *Computers and Fluids*, Vol. 26, No. 6, 1997, pp. 635–659. doi:10.1016/S0045-7930(97)00014-5

[17] van Leer, B., "Towards the Ultimate Conservation Difference Scheme 2: Monotonicity and Conservation Combined in a Second Order Scheme," *Journal of Computational Physics*, Vol. 14, No. 4, March 1974, pp. 361–370. doi:10.1016/0021-9991(74)90019-9

[18] Wilcox, D. C., *Turbulence Modeling for CFD*, 2nd ed., DCW Industries, La Cañada Flintridge, CA, 1998.

[19] Wilcox, D. C., "Wall Matching, a Rational Alternative to Wall Functions," AIAA Paper 89-0611, Jan. 1989.

[20] Suresh, A., and Huynh, H. T., "Numerical Experiments on a New Class of Nonoscillatory Schemes," AIAA Paper 92-0421, Jan. 1992.

[21] Yoshizawa, A., and Horiuti, K., "A Statistically-Derived Subgrid Scale Kinetic Energy Model for the Large-Eddy Simulation of Turbulent Flows," *Journal of the Physical Society of Japan*, Vol. 54, Aug. 1985, pp. 2834–2839. doi:10.1143/JPSJ.54.2834

[22] Strelets, M., "Detached Eddy Simulation of Massively Separated Flows," AIAA Paper 2001-0879, Jan. 2001.

[23] Nikitin, N. V., Nicoud, F., Wasistho, B., Squires, K. D., and Spalart, P. R., "An Approach to Wall Modeling in Large-Eddy Simulations," *Physics of Fluids*, Vol. 12, No. 7, July 2000, pp. 1629–1632. doi:10.1063/1.870414

[24] Choi, J., Edwards, J. R., and Baurle, R. A., "Compressible Boundary Layer Predictions at High Reynolds Number Using Hybrid LES/RANS

Methods," AIAA Paper 2008-4175, June 2008.
[25] Hirsch, C., *Numerical Computation of Internal and External Flows*, Vol. 2, Wiley, New York, 1990.
[26] Ferziger, J. H., "Large Eddy Simulation," *ICASE/LaRC Short Course on Turbulent Flow Modeling and Prediction*, NASA Langley Research Center, Hampton, VA, March 1994.
[27] Tecplot 360, Release 2, http://www.tecplot.com/, Tecplot, Bellevue, WA, 2008.
[28] Xiao, X., Edwards, J. R., Hassan, H. A., and Baurle, R. A., "Inflow Boundary Conditions for Hybrid Large Eddy/Reynolds Averaged Navier-Stokes Simulations," *AIAA Journal*, Vol. 41, No. 8, Aug. 2003, pp. 1481–1489.
doi:10.2514/2.2130
[29] Sagaut, P., Garnier, E., Tromeur, E., Larchêveque, L., and Labourasse, E., "Turbulent Inflow Conditions for Large Eddy Simulation of Compressible Wall-Boundary Flows," *AIAA Journal*, Vol. 42, No. 3, 2004, pp. 469–477.
doi:10.2514/1.3461
[30] Xu, S., and Martin, M. P., "Assessment of Inflow Boundary Conditions for Compressible Turbulent Boundary Layers," *Physics of Fluids*, Vol. 16, No. 7, 2004, pp. 2623–2639.
doi:10.1063/1.1758218

F. Ladeinde
Associate Editor